

Isabela Quintela Matos

**Solvation Free Energy Calculations of  
Molecules Mimicking Asphaltenes Using The  
SAFT- $\gamma$  Mie Force Field**

Rio de Janeiro

2018

Isabela Quintela Matos

# **Solvation Free Energy Calculations of Molecules Mimicking Asphaltenes Using The SAFT- $\gamma$ Mie Force Field**

Master's thesis presented to Engenharia de Processos Químicos e Bioquímicos graduate program, Escola de Química, Universidade Federal do Rio de Janeiro, as required for obtaining a Master's degree in Chemical Engineering.

Universidade Federal do Rio de Janeiro

Escola de Química

Engenharia de Processos Químicos e Bioquímicos Graduate Program

Supervisor: Charles Rubber de Almeida Abreu

Co-supervisor: Papa Matar Ndiaye

Rio de Janeiro

2018

Isabela Quintela Matos

Solvation Free Energy Calculations of Molecules Mimicking Asphaltenes Using The SAFT- $\gamma$  Mie Force Field/ Isabela Quintela Matos. – Rio de Janeiro, 2018-

69

Supervisor: Charles Rubber de Almeida Abreu

Dissertation (Master) – Universidade Federal do Rio de Janeiro  
Escola de Química

Engenharia de Processos Químicos e Bioquímicos Graduate Program, 2018.

1. Solvation free energy. 2. Asphaltenes. 3. SAFT- $\gamma$  Mie force field.

Isabela Quintela Matos

# **Solvation Free Energy Calculations of Molecules Mimicking Asphaltenes Using The SAFT- $\gamma$ Mie Force Field**

Master's thesis presented to Engenharia de Processos Químicos e Bioquímicos graduate program, Escola de Química, Universidade Federal do Rio de Janeiro, as required for obtaining a Master's degree in Chemical Engineering.

Approved dissertation. Rio de Janeiro, January 8, 2018:

---

**Charles Rubber de Almeida Abreu**  
Supervisor

---

**Professor**  
Guest 1

---

**Professor**  
Guest 2

---

**Professor**  
Guest 3

---

**Professor**  
Guest 4

Rio de Janeiro  
2018

# Abstract

This dissertation studied the solvation free energy differences of molecules mimicking asphaltenes in different solvents with the SAFT- $\gamma$  Mie force field. Solvation free energy differences were obtained by carrying out molecular dynamics simulations at the expanded ensemble. The output from these simulations was then used to estimate the differences with the MBAR method. The results with solvents other than water had low absolute deviations in relation to the experimental data. Meanwhile, the hydration free energy calculations required a binary interaction parameter estimated with output data from molecular dynamics in order to obtain accurate free energy differences. These results indicated some problems on the SAFT- $\gamma$  Mie model for water, but, generally, proved that a coarse grained model can represent the free energy differences of the studied sets of solute-solvent.

**Keywords:** solvation free energy. asphaltenes. SAFT- $\gamma$  Mie force field.

# List of Figures

2.2.1	Thermodynamic cycle for solvation free energy calculations with molecular dynamics (Adapted from Klimovich, Shirts and Mobley (2015)) . . .	14
3.1.1	Values for parameter $\chi$ according to the ring geometry (MÜLLER; MEJÍA, 2017) . . . . .	22
4.1.1	Geometry for $m_s = 5$ . . . . .	30
4.1.2	Geometry for $m_s = 3$ . . . . .	30
5.1.1	Solvation free energy profiles of different solutes in hexane. . . . .	35
5.1.2	Solvation free energy profiles of different solutes in 1-octanol. . . . .	35
5.1.3	Solvation free energy profiles of different solutes in toluene. . . . .	36
5.1.4	Solvation free energy profiles of phenanthrene in toluene+ $CO_2$ . . . . .	37
5.2.1	Hydration free energy profiles for different solutes. . . . .	39
B.0.1	Overlapping matrix for hexane+benzene. . . . .	53
B.0.2	Overlapping matrix for hexane+pyrene. . . . .	54
B.0.3	Overlapping matrix for hexane+phenanthrene. . . . .	55
B.0.4	Overlapping matrix for 1-octanol+propane. . . . .	56
B.0.5	Overlapping matrix for 1-octanol+anthracene. . . . .	57
B.0.6	Overlapping matrix for 1-octanol+phenanthrene. . . . .	58
B.0.7	Overlapping matrix for toluene+pyrene. . . . .	59
B.0.8	Overlapping matrix for toluene+anthracene. . . . .	60
B.0.9	Overlapping matrix for toluene+phenanthrene. . . . .	61
B.0.10	Overlapping matrix for toluene+ $CO_2$ (0.087)+phenanthrene. . . . .	62
B.0.11	Overlapping matrix for toluene+ $CO_2$ (0.119)+phenanthrene. . . . .	63
B.0.12	Overlapping matrix for toluene+ $CO_2$ (0.169)+phenanthrene. . . . .	64
B.0.13	Overlapping matrix for toluene+ $CO_2$ (0.289)+phenanthrene. . . . .	65
B.0.14	Overlapping matrix for water+propane. . . . .	66
B.0.15	Overlapping matrix for water+benzene. . . . .	67
B.0.16	Overlapping matrix for water+toluene. . . . .	68
B.0.17	Overlapping matrix for water+phenanthrene. . . . .	69

# List of Tables

Table 1 – Estimated SAFT- $\gamma$ Mie Force Field parameters for phenanthrene . . . .	33
Table 2 – SAFT- $\gamma$ Mie Force Field for each substance used in this work . . . . .	33
Table 3 – Calculated and experimental values for the solvation free energy differences (kcal/mol) of solutes in non aqueous solvents . . . . .	34
Table 4 – Calculated values for the solvation free energy differences (kcal/mol) of phenanthrene in toluene+ $CO_2$ . . . . .	36
Table 5 – Calculated values for the hydration free energy differences (kcal/mol) of solutes in water for $k_{ij} = 0$ . . . . .	38
Table 6 – Binary interaction parameters employed. . . . .	38
Table 7 – Calculated and experimental values for the hydration free energy differences (kcal/mol) of solutes in water. . . . .	39
Table 8 – Optimized values of $\lambda$ and $\eta$ for the solutes in hexane . . . . .	50
Table 9 – Optimized values of $\lambda$ and $\eta$ for the solutes in 1-octanol . . . . .	51
Table 10 – Optimized values of $\lambda$ and $\eta$ for the solutes in toluene . . . . .	51
Table 11 – Optimized values of $\lambda$ and $\eta$ for the phenanthrene in different mass fractions of $CO_2$ in toluene . . . . .	52
Table 12 – Optimized values of $\lambda$ and $\eta$ for the solutes in water . . . . .	52

# Contents

<b>1</b>	<b>INTRODUCTION</b>	<b>9</b>
<b>2</b>	<b>LITERATURE REVIEW</b>	<b>11</b>
<b>2.1</b>	<b>Coarse Grained Force Fields</b>	<b>11</b>
<b>2.2</b>	<b>Solvation Free Energies Based on Molecular Dynamics</b>	<b>13</b>
<b>2.3</b>	<b>Post simulation methods</b>	<b>16</b>
2.3.1	Thermodynamic integration	16
2.3.2	Free Energy of Perturbation (FEP)	16
2.3.3	Bennet Acceptance Ratio (BAR)	17
2.3.4	Multistate Bennet Acceptance Ratio (MBAR)	18
<b>3</b>	<b>FUNDAMENTALS OF THE COMPUTATIONAL METHODS</b>	<b>19</b>
<b>3.1</b>	<b>SAFT-<math>\gamma</math> Mie Force Field</b>	<b>19</b>
3.1.1	SAFT-VR Mie EoS	19
3.1.1.1	Ideal Contribution	19
3.1.1.2	Monomer Contribution	20
3.1.1.3	Chain Contribution	20
3.1.1.4	Ring Contribution	21
3.1.1.5	Combining rules for the intermolecular potential parameters	21
3.1.2	Parameter Estimation for the SAFT- $\gamma$ Mie Force Field	22
<b>3.2</b>	<b>Molecular Dynamics</b>	<b>25</b>
<b>3.3</b>	<b>Expanded Ensemble Method</b>	<b>25</b>
<b>3.4</b>	<b>Gibbs Ensemble Monte Carlo (GEMC)</b>	<b>28</b>
<b>4</b>	<b>METHODOLOGY</b>	<b>30</b>
<b>4.1</b>	<b>Phenanthrene Parameterization</b>	<b>30</b>
<b>4.2</b>	<b>Solvation Free Energy Calculations</b>	<b>31</b>
<b>5</b>	<b>RESULTS AND DISCUSSION</b>	<b>33</b>
<b>5.1</b>	<b>Solvation free energies</b>	<b>33</b>
<b>5.2</b>	<b>Hydration free energies</b>	<b>37</b>
<b>6</b>	<b>CONCLUSIONS</b>	<b>40</b>
	<b>BIBLIOGRAPHY</b>	<b>42</b>



<b>APPENDIX</b>	<b>49</b>
<b>APPENDIX A – OPTIMIZED VALUES OF <math>\lambda</math> AND <math>\eta</math> . . . . .</b>	<b>50</b>
<b>APPENDIX B – OVERLAPPING MATRICES . . . . .</b>	<b>53</b>

# 1 Introduction

Solvation free energy calculations with molecular dynamics (MD) have a variety of applications ranging from drug design in the pharmaceutical industry to development of separation technologies in the chemical industry. Solvation free energy is, more specifically, the Gibbs free energy difference between the solute alone in the gas phase and the solute interacting with the solvent. Through the study of this solvation phenomenon, it is possible to obtain information about the behavior of the solvent in different chemical environments and the influence of the solute's molecular geometry. It is also possible to calculate other important properties with the solvation free energy, namely the activity coefficient at infinite dilution, Henry constant, partition coefficients and solubility.

The solvation phenomenon is intrinsically complex. There are many competing forces interfering in the behavior of the solute-solvent interaction and free energy simulations are susceptible to sampling problems for high energy regions. With the intention of improving free energy calculations, simulation methodologies such as the expanded ensemble (LYUBARTSEV *et al.*, 1992), thermodynamic integration (KIRKWOOD, 1935), free energy perturbation (ZWANZIG, 1954; BENNETT, 1976; SHIRTS; CHODERA, 2008) and umbrella sampling (TORRIE; VALLEAU, 1977) have been developed in order to obtain accurate estimations for the energy differences.

Another influencing factor in the output of these calculations are the force fields chosen to describe the solvent and solute molecules. Force fields have different levels of description (quantum mechanics, atomistic, coarse grained). In the coarse grained description, molecules are grouped in pseudo atoms or beads. Coarse grained models generally reproduce free energy differences since the effects of reducing degrees of freedom in the entropy are counterbalanced by the reduction of enthalpic terms (KMIECIK *et al.*, 2016). Additionally, the success of a coarse grained force field is important to increase the scale of solvation free energy calculations and reveal deficiencies in the description of small molecules by these models (MOBLEY *et al.*, 2007; SHIRTS *et al.*, 2003). That's the reason we, at this study, try to provide information about free energy calculation on the expanded ensemble with the SAFT- $\gamma$  Mie coarse grained force field. This force field uses the Mie Potential (MIE, 1903) and has a more straightforward method of obtaining its parameters than other models. It was initially parameterized with pure component equilibrium and interfacial tension data. This strategy has provided satisfactory results for prediction of phase equilibrium of aromatic compounds, alkanes, light gases and water (HERDES; TOTTON; MÜLLER, 2015; MÜLLER; MEJÍA, 2017; LOBANOVA *et al.*, 2015), thermodynamic properties of carbon dioxide and

methane (AIMOLI; MAGINN; ABREU, 2014a), multiphase equilibrium of mixtures of water, carbon dioxide and n-alkanes (LOBANOVA *et al.*, 2016) and water/oil interfacial tension (HERDES *et al.*, 2017).

The solvents and solutes chosen in this study range from standard sets used as benchmark in solvation free energy calculations to ring substances used as a model to asphaltenes. Asphaltenes are complicated to characterize by determining their composition on a molecular basis, but it is generally accepted that they can be characterized as a fraction of crude oil soluble in toluene and insoluble in n-alkenes (pentane, hexane, heptane) (SJÖBLOM *et al.*, 2003). They've motivated many studies interested in developing models for their structure due to all the problems they can cause during their transportation and refining (SJÖBLOM; SIMON; XU, 2015). This work's strategy to test the efficiency of the SAFT- $\gamma$  Mie force field in describing the solvation phenomenon was to use molecules that appear in asphaltenes models and that have similarities in terms of solubilities with asphaltenes (phenanthrene, anthracene, pyrene) for the solutes. Meanwhile, for the solvents, we chose compounds that are used to characterize asphaltenes (toluene, hexane). The anti solvent/solvent effect of carbon dioxide was also tested due to its influence in asphaltene precipitation during the oil processing (SOROUSH *et al.*, 2014). Asphaltenes are described by their solubility, hence simulation scale can be increased and studies with more complete models can be carried out if this coarse grained model can correctly describe solvation free energy differences of simple molecules mimicking asphaltenes.

## 2 Literature Review

### 2.1 Coarse Grained Force Fields

Molecular simulations can be carried out at different levels of description. The detailed atomistic level or *ab initio* level is described by the laws of quantum mechanics. The system consists of a set of subatomic particles in which Schrodinger's equation is solved for all of them. The next level is the atomistic description. It considers that the system is made up of atoms following the laws of statistical mechanics. Force fields at this level are based on pair potentials with Coulombic charged sites. Contributions due to intramolecular interactions such as bond-stretching, angle-bending and torsion are also usually accounted by these kinds of force fields. When the simulation scale needs to be increased and the atomistic simulations become too computationally expensive, the coarse-grained (CG) description is more suited. It considers that the system is made up of pseudo atoms or beads that contain multiple atoms or even an entire molecule.

There is an obvious loss of information in grouping atoms, hence it is necessary to assure that the process of eliminating unnecessary or unimportant information ('coarse graining') doesn't affect the system's physical behavior. Ideally, coarse grained models need to have accuracy, transferability, robustness, and computational efficiency. In order to achieve these goals, coarse grained force fields are usually developed by mapping the atomistic model in order to define the pseudo atoms, which are generally formed by similar functional groups. The level of coarse graining also needs to be defined, up to 6 heavy atoms (non-hydrogen atoms) per bead in order to not lose important details and maintain isotropic representations of the beads (SHINODA; DEVANE; KLEIN, 2007; MARRINK *et al.*, 2007; HADLEY; MCCABE, 2012). CG force fields can be parametrized following two different approaches: bottoms up and top down. The bottoms up approach uses information of a more detailed scale such as the *ab initio* description or the atomistic description to obtain information necessary to the parametrization. This method highly depends on the detailed model quality to succeed. Meanwhile, the top down methodology obtains parameters from larger scales, namely experimental thermodynamic properties or native-structure based properties.

One of the first applications of coarse grained models is the study of protein folding (LEVITT; WARSHE, 1975; LEVITT, 1976). These earlier protein CG models were based on molecule structure, and they contributed for the knowledge of physicochemical forces associated with protein folding and protein interactions (KOGA; TAKADA, 2001). More recent, models focused on retaining the protein's chemical specificity. The Bereau and Deresmo model (BEREAU; DESERNO, 2009) has up to four-bead representation

and was used in studies of protein folding and aggregation. However, this model still needs tuning to improve protein stability (BEREAU; BACHMANN; DESERNO, 2010). The OPEP (Optimized Potential for Efficient Protein Structure Prediction) model (STERPONE *et al.*, 2014; STERPONE; DERREUMAUX; MELCHIONNA, 2015) has up to six-bead representation. It was used to investigate a variety of phenomenon, ranging from protein folding to *ab initio* peptide structure prediction (BARDUCCI; BONOMI; DERREUMAUX, 2011; CHEBARO *et al.*, 2009b; CHEBARO *et al.*, 2009a). Another CG protein models used in the literature are the Scorpion (solvated coarse-grained protein interaction) (BASDEVANT; BORGIS; HA-DUONG, 2013), the UNRES (united residue) (ADAM *et al.*, 2014) and the MARTINI model (LARS *et al.*, 2013). The later one is the most popular model for CG modeling of membrane proteins (MARRINK; TIELEMAN, 2013). The MARTINI model is also extensively used as CG model for water. This model represents four water molecules as one bead using a shifted Lennard Jones potential for non bonded interactions. Though its extensive use, the MARTINI water model doesn't properly represent properties as interfacial tension and compressibility (HE *et al.*, 2010) and can freeze at room temperature (WINGER *et al.*, 2009; MARRINK *et al.*, 2007), what requires the use of anti-freeze agents during the simulations. This behavior can be explained by the high level of coarse graining (4:1), the lack of explicit charges and the use of a 12-6 potential. Chiu, Scott and Jakobsson (2010) used the Morse Potential, which is softer than the LJ potential, to improve the MARTINI model. Meanwhile, Shinoda, Devane and Klein (2007) used different forms of the Mie potential. They concluded that a 12-4 Mie Potential was ideal for water cross interactions and a 9-6 Mie Potential was suited for solute-solute interactions.

Outside of the Martini framework, He *et al.* (2010) studied different levels of coarse-graining for water ranging for one to 4 molecules per bead using different Mie and Morse potentials. Works also assessed the use of Soft-core potentials to study aqueous solutions of surfactants (SHINODA; DEVANE; KLEIN, 2007), ionic liquids (BHARGAVA; KLEIN, 2009), lipids (SHINODA; DEVANE; KLEIN, 2010) and membranes (PANTANO; KLEIN, 2009). Another CG force field for water based on the Mie Potential is the SAFT- $\gamma$  Mie (LOBANOVA *et al.*, 2015). In this strategy, there are two different models: the CGW1-vle and the CGW1-ift. Both of them represent the water molecule as one bead and the Mie Potential has a repulsive and attractive parameter equal to eight and six, respectively. The CGW1-vle model was parameterized using saturated-liquid density and vapor pressure data, and should be used for simulations of aqueous systems' fluid-phase equilibrium at high temperatures and pressures. This model still suffers from premature freezing with a triple point at 343 K. The other model, CGW1-ift, was parameterized using saturated-liquid density and vapor-liquid interfacial tension, hence it is best suited for interfacial properties calculations. Both models have temperature-dependent size and energy parameters and performed well for these

properties over the entire liquid temperature range. The SAFT- $\gamma$  Mie force field have also been applied to other compounds with satisfactory results. Müller and Mejía (2017) parameterized the force field for aromatic compounds and tested it with simulations of fluid phase equilibrium. Herdes, Totton and Müller (2015) carried out simulations of alkanes and light gases. Binary and ternary mixtures of water, carbon-dioxide and water (LOBANOVA *et al.*, 2016), thermodynamic and transport properties of carbon dioxide and methane (AIMOLI; MAGINN; ABREU, 2014a; AIMOLI; MAGINN; ABREU, 2014b) and water/oil interfacial tension (HERDES *et al.*, 2017) were also studied with this force field.

## 2.2 Solvation Free Energies Based on Molecular Dynamics

Free energies can be expressed as averages over ensembles of atomic configurations generated using Monte Carlo or molecular dynamics techniques. In the canonical ensemble, the free energy is given by:

$$F(N, V, T) = -\kappa_b T \ln Q(N, V, T) \quad (2.1)$$

where  $Q(N, V, T)$  is the partition function of the canonical ensemble:

$$Q(N, V, T) = \int d^n p d^n r \exp \left[ -\beta \left( \sum_{i=1}^N \frac{p_i^2}{2m_i} + U(r_1, \dots, r_n) \right) \right] \quad (2.2)$$

where  $\beta = 1/k_b T$ . Meanwhile, the average over the isothermal-isobaric ensemble gives the Gibbs free energy:

$$G(N, P, T) = -\kappa_b T \ln \Delta(N, P, T) \quad (2.3)$$

where  $\Delta(N, P, T)$  is the partition function of the isothermal-isobaric ensemble:

$$\Delta(N, P, T) = \frac{1}{V_0} \int_0^\infty dV \int d^n p d^n r \exp \left[ -\beta \left( \sum_{i=1}^N \frac{p_i^2}{2m_i} + U(r_1, \dots, r_n) + PV(r_1, \dots, r_n) \right) \right] \quad (2.4)$$

Since it is only possible to obtain free energy differences, solvation free energy calculations based on molecular dynamics estimate the difference between the Gibbs free energies of end states:

$$\Delta G_{AB} = G_B - G_A = -\kappa_b T \ln \left( \frac{\Delta_B}{\Delta_A} \right) = -\kappa_b T \ln \left( \frac{Z_B}{Z_A} \right) \quad (2.5)$$

As both states are at the same temperature, the moment integrals in the ratio  $\Delta_B/\Delta_A$  can be simplified. Therefore, this ratio becomes equal to the ratio of the configuration partition functions:

$$\frac{Z_B}{Z_A} = \frac{\int_0^\infty dV \int d^n r \exp[-\beta (U(r_1, \dots, r_n) + PV(r_1, \dots, r_n))]_B}{\int_0^\infty dV \int d^n r \exp[-\beta (U(r_1, \dots, r_n) + PV(r_1, \dots, r_n))]_A} \quad (2.6)$$

The Gibbs free energy difference between end states  $A$  and  $B$  are, more specifically, the difference between the solute alone in the gas phase and the solute interacting with the solvent. In order to these differences be accurate, the states' phase integral must have sufficient overlap (KLIMOVICH; SHIRTS; MOBLEY, 2015). This can be achieved by calculating the free energy difference between a series of intermediates states. The result of these differences are independent of the path chosen since free energy is a state function. That's why alchemical states (no physical sense) are used to link physical states of interest. The solvation free energy calculations are done through a thermodynamic cycle to gradually insert the solute molecule into the solvent as illustrated in Figure 2.2.1. According to this cycle, the free energy of solvation is expressed as:

$$\Delta G_{solv} = \Delta G_{1 \rightarrow 4} = \Delta G_{1 \rightarrow 2} + \Delta G_{2 \rightarrow 3} + \Delta G_{3 \rightarrow 4} \quad (2.7)$$

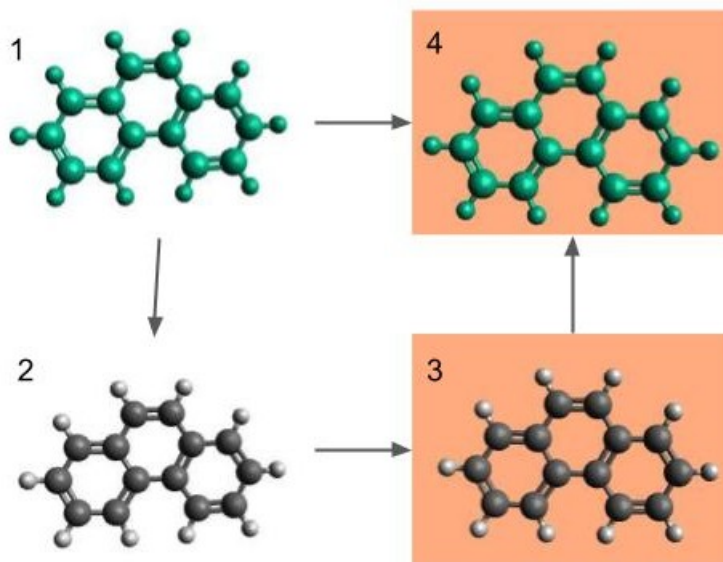


Figure 2.2.1 – Thermodynamic cycle for solvation free energy calculations with molecular dynamics (Adapted from Klimovich, Shirts and Mobley (2015))

The solvation free energy between states 1 and 2 in Figure 2.2.1 is associated with turning off the molecule's non bonded interactions in the gas phase. The following transformation,  $\Delta G_{2 \rightarrow 3}$ , is the free energy of moving the non-interacting molecule in the gas phase to the solvent, and is equal to zero since the transformation of a non-interacting molecule doesn't depend on the environment. Lastly,  $\Delta G_{3 \rightarrow 4}$  is the free



energy required to the non-interaction molecule in the aqueous phase regain its non-bonded interactions. The solvation free energy calculation can be classified according to the types of non bonded interactions that are turned off in the  $1 \rightarrow 2$  and  $3 \rightarrow 4$  parts of the cycle. If both non-bonded interactions with the environment and internal interactions are turned off, this is an annihilation free energy calculation. Meanwhile, if only non-bonded interactions with the environment are turned off, this is a decoupling free energy calculation. In the later case,  $\Delta G_{1 \rightarrow 2} = 0$  and the  $\Delta G_{solv} = \Delta G_{3 \rightarrow 4}$ . The methods used to carry out these transformations scale the solute charges to zero and then turn off the interactions corresponding to the Lennard Jones potential. In order to carry out the later process, a modified potential with a coupling parameter( $\lambda$ ) is used. Each  $\lambda$  represent an alchemical state and, when  $\lambda = 0$ , there is no interaction with the solvent and, when  $\lambda = 1$ , interactions are fully activated. The coupling of the  $\lambda$  parameter could be linear, but it could generate numerical problems related to the exponential part of the potential. That's why the non-linear soft-core scheme (BEUTLER *et al.*, 1994) is usually used, the generalized soft core potential is given by:

$$U^{sc}(r) = \lambda \epsilon \frac{\lambda_r}{\lambda_r - \lambda_a} \left( \frac{\lambda_r}{\lambda_a} \right)^{\left( \frac{\lambda_a}{\lambda_r - \lambda_a} \right)} \left\{ \frac{1}{[\alpha(1 - \lambda) + (r/\sigma)^{\lambda_a}]^{\lambda_r/\lambda_a}} - \frac{1}{\alpha(1 - \lambda) + (r/\sigma)^{\lambda_a}} \right\} \quad (2.8)$$

Using the Lennard Jones exponents, Eq. (2.8) becomes:

$$U_{LJ}^{sc}(r) = 4\lambda \epsilon \left\{ \frac{1}{[\alpha(1 - \lambda) + (r/\sigma)^6]^2} - \frac{1}{\alpha(1 - \lambda) + (r/\sigma)^6} \right\} \quad (2.9)$$

where  $\alpha$  is a constant which the value of 0.5 is normally assumed to it. The  $\Delta G_{3 \rightarrow 4}$  can be then obtained by doing independent simulations in different values of  $\lambda$  or by doing expanded ensemble simulations (LYUBARTSEV *et al.*, 1992), which samples all states in a single simulation. This method allows a faster sampling across the alchemical states, provided that the kinetic barriers are not substantial. The free energies of solvation obtained can then be used to calculate other properties such as the partition coefficient, that is a measure of the partitioning of one solute in two solvents (a and b) at a temperature T:

$$\log P^{a/b} = \frac{\Delta G_{solv}^a - \Delta G_{solv}^b}{2.303RT} \quad (2.10)$$

Using the methodology described above, a variety of work about free nergy calculations have been published. Recently, Mobley and Guthrie (2014), Matos *et al.* (2017) made available a big database of hydration free energy of small molecules using the GAFF force field. A comparison of polar and nonpolar contributions to these



hydration free energy indicated the significance of each terms (IZAIRI; KAMBERAJ, 2017). Garrido *et al.* (2009), Garrido *et al.* (2011) calculated the free energy of solvation of large alkanes in 1-octanol and water with three different force fields (TraPPE, Gromos, OPLS-AA/TraPPE) and the solvation free energy of propane and benzene in non aqueous solvents like n-hexadecane, n-hexane, ethyl benzene, acetone with the force fields TraPPE-UA and TraPPE-AA. Roy, Blinov and Kovalenko (2017) addressed the choice of the Lennard Jones parameters for predicting solvation free energy in 1-octanol. Gonçalves and Stassen (2005) calculated the free energy of solvation in the solvents tetrachloride, chloroform and benzene with GROMOS force field. Using the GAFF and the polarizable AMOEBA force fields, Mohamed, Bradshaw and Essex (2016) evaluated the solvation free energy of small molecules in toluene, chloroform and acetonitrile and obtained a mean unsigned error of 1.22 *kcal/mol* for the AMOEBA and 0.66 *kcal/mol* for the GAFF.

## 2.3 Post simulation methods

The data from molecular dynamics simulations method explained in the section above provide the potential energies corresponding to each  $\lambda$ . These potential energies obtained need to be post processed and analyzed in order to calculate the solvation free energies. Some widely used methods for these calculations are going to be briefly described below.

### 2.3.1 Thermodynamic integration

The thermodynamic integration method (KIRKWOOD, 1935) uses equilibrium averages to evaluate the potential energy derivative with respect to the coupling parameter. Then, the free energies are obtained as the integration of the initial and final state derivatives:

$$\Delta G_{solv} = \int_0^1 \frac{\partial U}{\partial \lambda} d\lambda \quad (2.11)$$

The integral in Eq. (2.11) is obtained by interpolating the output data from simulations in different ways. Some examples of methods for the interpolations are the trapezoidal rule or natural cubic spline (PALIWAL; SHIRTS, 2011). There are also more complex schemes that are usually system specific as the works of Jorge *et al.* (2010) and Shyu and Ytreberg (2010).

### 2.3.2 Free Energy of Perturbation (FEP)

The free energy of perturbation method (ZWANZIG, 1954) is the oldest and one of the most general purpose strategy to calculate free energy differences. In this method, the difference between two thermodynamic states A and B is given by:

$$\Delta G_{AB} = -\frac{1}{\beta} \ln \langle e^{-\beta(U_B - U_A)} \rangle_A \quad (2.12)$$

According to the equation above, the free energy difference is calculated by doing an average over the potential energies of state A and B obtained during the simulation of state A. This method requires a great overlap between states (the state B needs to represent a small perturbation in state A) in order to obtain a rapid convergence of the free energy difference. To assure overlap, it is possible to carry out simulations in N intermediate states between A and B, so Eq. (2.12) becomes:

$$\Delta G_{AB} = -\frac{1}{\beta} \ln \left( \frac{1}{N} \sum_{i=0}^{N+1} e^{-\beta(U_{i+1} - U_i)} \right) \quad (2.13)$$

The way of calculating  $\Delta G$  of Eq. (2.13) is called Exponential Averaging (EXP) (ZWANZIG, 1955; PALIWAL; SHIRTS, 2011). The direction of the transformation is also important in this method. If the direction is of decreasing entropy, the step is of insertion ( $\Delta G_{AB}$ ) and the method is called insertion exponential averaging (IEXP). The direction of increasing entropy is called a deletion step ( $\Delta G_{BA}$ ) and the method is labeled as deletion exponential averaging (DEXP). These directions can yield different values of free energy differences due to under sampling in the tail regions of the  $\Delta G_{AB}$  distribution (KLIMOVICH; SHIRTS; MOBLEY, 2015; POHORILLE; JARZYNSKI; CHIPOT, 2010). These problems make the EXP methods not suited to calculate free energy differences when the system hasn't a sufficient overlap. For these cases, the Bennet Acceptance Ratio or the Multi-State Bennet Acceptance Ratio is more indicated.

### 2.3.3 Bennet Acceptance Ratio (BAR)

The BAR method (BENNETT, 1976) was developed with the intent of eliminating the bias in the free energy estimation. It uses the uncorrelated samples of the potential energy in both directions ( $A \rightarrow B$  and  $B \rightarrow A$ ) to obtain the free energy differences using the information in a statically optimal way. The free energy difference between two intermediate states (i and j) is calculated by the self-consistent solution of the following

equations:

$$\Delta G_{ij} = \frac{1}{\beta} \ln \left( \frac{\sum_{k=1}^{N_j} \frac{1}{1 + \exp[-\beta(\Delta U_k^j - C)]}}{\sum_{l=1}^{N_i} \frac{1}{1 + \exp[-\beta(\Delta U_l^i - C)]}} \right) + C - \frac{1}{\beta} \ln \left( \frac{N_j}{N_i} \right) \quad (2.14)$$

$$C = \Delta G_{ij} + \frac{1}{\beta} \ln \left( \frac{N_j}{N_i} \right) \quad (2.15)$$

The total free energy difference between end states is then given by the sum over differences of consecutive intermediate states. This method also provides a function to obtain the minimum variance for free energy differences. The variance equation for any value of  $C$  is given by:

$$s_{ij}^2 = \frac{1}{\beta^2 N_i} \left[ \frac{\langle f^2(x) \rangle_i}{\langle f(x) \rangle_i^2} - 1 \right] + \frac{1}{\beta^2 N_j} \left[ \frac{\langle f^2(x) \rangle_j}{\langle f(x) \rangle_j^2} - 1 \right] \quad (2.16)$$

where  $f(x) = 1/(1+x)$  is the Fermi equation and  $x = \exp[\beta(\Delta U - C)]$ . The variance of the free energy difference between end states can be calculated by assuming independent errors and summing over the variance of consecutive intermediate states. However, this assumption is not correct and there is no general formula to obtain a statistically unbiased estimate of an entire transformation with the BAR method (PALIWAL; SHIRTS, 2011).

There are two other methods related to the BAR method that don't solve Eqs. (2.14) and (2.15) self consistently. By doing that, free energy differences will not have minimum variance, but significant space and disk memory can be saved since the averages of Eqs. (2.14) - (2.16) are accumulated. The two methods are the Unoptimized Bennett Acceptance Ratio (UBAR) and the Range-Based Bennett Acceptance Ratio (RBAR). The first one avoids the self consistently resolution of the BAR equations by defining  $C = \beta^{-1} \ln(N_j/N_i)$ . The UBAR method also requires that the intermediate free energy differences are approximately equal to zero to obtain optimal estimations. Meanwhile, the RBAR method selects a range of initial guesses of the constant  $C$  in order to calculate a range of  $\Delta G_{ij}$ . The value of free energy difference correspondent to the minimum variance is then used as input in Eq. (2.15) to calculate the value of  $C$ . Hence, this method requires a good estimation of the initial range for the values of  $C$ . In terms of accuracy, the UBAR method can be as accurate as the BAR method, but it may end up being as computational costly (PALIWAL; SHIRTS, 2011).

### 2.3.4 Multistate Bennet Acceptance Ratio (MBAR)

The MBAR method (SHIRTS; CHODERA, 2008) is a further development of the BAR method. It proposes an estimator that computes free energies and their uncertainties of all  $K$  states by minimizing the  $K \times K$  matrix of variances simultaneously. The estimator solves the following equation for each  $G_i$  self consistently:

$$G_i = \frac{1}{\beta} \ln \sum_{k=1}^K \sum_{n=1}^{N_k} \frac{\exp[-\beta U_i(x_{kn})]}{\sum_{l=1}^K N_l \exp[\beta(G_l - U_l(x_{kn}))]} \quad (2.17)$$

The equation above requires the evaluation of the potential energy of uncorrelated configuration  $n$  for all  $K$  states ( $U_i(x_{kn})$ ) and for all uncorrelated configuration snapshots ( $N_k$ ) from state  $k$ . Free energy changes between states are given then by  $\Delta G_{ij} = G_j - G_i$ . The statistical variance of  $S_{ij}^2 \Delta G_{ij}$  is given by the matrix covariances:

$$s_{ij}^2 \Delta G_{ij} \equiv \text{cov}(-\ln \hat{Z}_j / \hat{Z}_i, -\ln \hat{Z}_j / \hat{Z}_i) \quad (2.18)$$

where  $\hat{Z}_j$  and  $\hat{Z}_i$  are the partition functions of states  $i$  and  $j$ . The MBAR method can be considered as limit case of the Weighted Histogram Analysis Method (WHAM) (KUMAR *et al.*, 1992) for computing free energies. Eq. (2.17) becomes equal to the WHAM equations if the histogram width tend to zero. Despite this, the MBAR is still more suited because it doesn't have the bias associated with the discretization and it allows the calculation of an error estimate.

## 3 Fundamentals of the Computational Methods

### 3.1 SAFT- $\gamma$ Mie Force Field

#### 3.1.1 SAFT-VR Mie EoS

The SAFT-VR Mie equation of state (LAFITTE *et al.*, 2013) is the basis for the SAFT- $\gamma$  Mie coarse grained force field (AVENDAÑO *et al.*, 2011). This EoS was initially developed to describe chain molecule formed from fused Mie segments using the Mie attractive and repulsive potential. The Mie potential is a type of generalized Lennard-Jones potential that can be used to explicitly describe repulsive interactions of different hardness/softness and attractive interactions of different ranges, and is given by:

$$U_{Mie}(r) = \epsilon \frac{\lambda_r}{\lambda_r - \lambda_a} \left( \frac{\lambda_r}{\lambda_a} \right)^{\left( \frac{\lambda_a}{\lambda_r - \lambda_a} \right)} \left[ \left( \frac{\sigma}{r} \right)^{\lambda_r} - \left( \frac{\sigma}{r} \right)^{\lambda_a} \right] \quad (3.1)$$

where  $\epsilon$  is the potential well depth,  $\sigma$  is the segment diameter,  $r$  is the distance between spherical segments,  $\lambda_r$  is the repulsive exponent and  $\lambda_a$  is the attractive exponent. This equation uses the Barker and Henderson (1976) high perturbation expansion of the Helmholtz free energy up to third order and an improved expression for the radial distribution function (RDF) of Mie monomers at contact to obtain an equation able to give an accurate theoretical description of the vapor-liquid equilibrium and second derivative properties (LAFITTE *et al.*, 2013). For a non-associating fluid, the Helmholtz free energy is:

$$\frac{A}{N\kappa_b T} = a = a^{IDEAL} + a^{MONO} + a^{CHAIN} \quad (3.2)$$

##### 3.1.1.1 Ideal Contribution

The ideal contribution for a mixture is given by:

$$a^{IDEAL} = \sum_{i=1}^{N_c} x_i \ln(\rho_i \Lambda_i^3) - 1 \quad (3.3)$$

where  $x_i = N_i/N$  is the molar fraction of component  $i$ ,  $\rho_i = N_i/V$  is the number density,  $N_i$  is the number of molecules of each component and  $\Lambda_i^3$  is the de Broglie wavelength.

### 3.1.1.2 Monomer Contribution

The monomer contribution describes interactions between Mie segments and can be expressed, for a mixture, as:

$$a^{MONO} = \left( \sum_{i=1}^{N_c} x_i m_{s,i} \right) a^M \quad (3.4)$$

In the equation above,  $m_{s,i}$  is the number of spherical segments making up the molecule  $i$  and  $a^M$  is the monomer dimensionless Helmholtz free energy and it is expressed as a third order perturbation expansion in the inverse temperature (BARKER; HENDERSON, 1976):

$$a^M = a^{HS} + \beta a_1 + \beta a_2^2 + \beta a_3^3 \quad (3.5)$$

where  $\beta = \kappa_b T$  and  $a^{HS}$  is the hard-sphere dimensionless Helmholtz free energy for a mixture :

$$a^{HS} = \frac{6}{\pi \rho_s} \left[ \left( \frac{\zeta_2^3}{\zeta_3^2} - \zeta_0 \right) \ln(1 - \zeta_3) + \frac{3\zeta_1\zeta_2}{1 - \zeta_3} + \frac{\zeta_2^3}{\zeta_3(1 - \zeta_3)^2} \right] \quad (3.6)$$

The variable  $\rho_s = \rho \sum_i^{N_c} x_i m_{s,i}$  is the total number density of spherical segments and  $\zeta_l$  are the moments of the number density:

$$\zeta_l = \frac{\pi \rho_s}{6} \left( \sum_{i=1}^{N_c} x_{s,i} d_{ii}^l \right), l = 0, 1, 2, 3 \quad (3.7)$$

where  $x_{s,i}$  is the mole fraction of segments and is related through the mole fraction of component  $i$  ( $x_i$ ) by:

$$x_{s,i} = \frac{m_{s,i} x_i}{\sum_{k=1}^{N_c} m_{s,k} x_k} \quad (3.8)$$

The effective hard-sphere diameter  $d_{ii}$  for the segments is:

$$d_{ii} = \int_0^{\sigma_{ii}} (1 - \exp(-\beta U_{ii}^{Mie}(r))) dr \quad (3.9)$$

The integral in Eq. (3.9) is normally obtained by means of Gauss-Legendre with a 5-point quadrature (PAPAIIOANNOU *et al.*, 2014). The detailing of terms of Eq. (3.4) can be found in Lafitte *et al.* (2013).

### 3.1.1.3 Chain Contribution

The chain formation of  $m_s$  tangentially bonded Mie segments contribution is based on the first-order perturbation theory (TPT1) (PAPAIIOANNOU *et al.*, 2014) and can be expressed as:

$$a^{CHAIN} = - \sum_{i=1}^{N_c} x_i (m_{s,i} - 1) \ln(g_{ii}^{Mie}(\sigma_{ii})) \quad (3.10)$$

The  $g_{ij}^{Mie}(\sigma_{ij})$  term correspond to the radial distribution function (RDF) of the hypothetical Mie system evaluated at the effective diameter and can be obtained with the perturbation expansion:

$$g_{ij}^{Mie}(\sigma_{ij}) = g_{d,ij}^{HS}(\sigma_{ij}) \exp[\beta \epsilon g_{1,ij}(\sigma_{ij})/g_{d,ij}^{HS}(\sigma_{ij}) + (\beta \epsilon)^2 g_{2,ij}(\sigma_{ij})/g_{d,ij}^{HS}(\sigma_{ij})] \quad (3.11)$$

The other terms in the equations above are explicitly exposed in the original article (LAFITTE *et al.*, 2013).

#### 3.1.1.4 Ring Contribution

There are two forms for the Helmholtz free energy for rings formed from  $m_s$  tangentially bonded segments in the literature. The first one (LAFITTE *et al.*, 2012) considered that the difference between a chain and a ring molecule is that the latter has one more bond that is connecting the first segment to the last. With this assumption, Eq. (3.10) can be adapted to rings by:

$$a^{RING} = - \sum_{i=1}^{N_c} x_i m_{s,i} \ln(g_{ii}^{Mie}(\sigma_{ii})) \quad (3.12)$$

According to Lafitte *et al.* (2012), Eq. (3.12) needs an additional parameterization with molecular simulation data so the EoS can be used in molecular simulations, but this procedure is not necessary for chain molecules. Recently, Müller and Mejía (2017) tried to correct this inconsistency by means of developing the ring free energy based on the work of Müller and Gubbins (1993), who obtained rigorous expressions for hard fluids with molecular geometries of rings of  $m_s = 3$ . The final expression developed for the ring dimensionless Helmholtz free energy is:

$$a^{RING} = - \sum_{i=1}^{N_c} x_i (m_{s,i} - 1 + \chi_i \eta_i) \ln(g_{ii}^{Mie}(\sigma_{ii})) \quad (3.13)$$

$\eta_i = m_{s,i} \rho_i \sigma_{ii}^3 / 6$  is the packing fraction and  $\chi_i$  is a parameter which depends on  $m_{s,i}$  and on the geometry of the ring of each component  $i$ . For a value of  $\chi = 0$ , Eq. (3.13) is equal to Eq. (3.10). Meanwhile, the equation corresponds to a hard sphere system of triangles when  $\chi = 1.3827$ . Müller and Mejía (2017) also calculated values of  $\zeta$  for  $m_s = 3, m_s = 4, m_s = 5, m_s = 7$  with pseudo-experimental data from molecular dynamics (MD) for a defined pure fluid. The values of  $\chi$  for each geometry estimated can be seen in Figure 3.1.1.

#### 3.1.1.5 Combining rules for the intermolecular potential parameters

Lafitte *et al.* (2013) also suggested mixing rules for the potential parameters based on Lorentz-Berthelot combining rules (ROWLINSON; SWINTON, 1982):

$$\sigma_{ij} = \frac{\sigma_{ii} + \sigma_{jj}}{2} \quad (3.14)$$

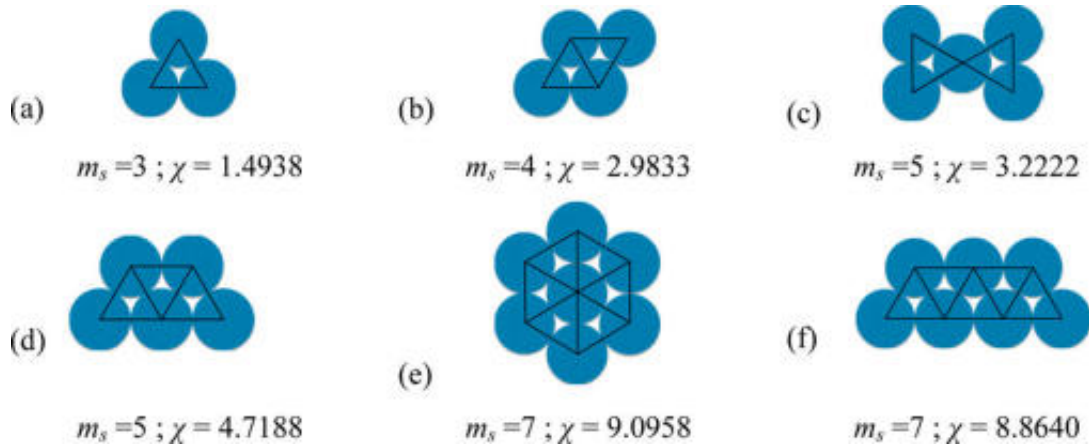


Figure 3.1.1 – Values for parameter  $\chi$  according to the ring geometry (MÜLLER; MEJÍA, 2017)

$$\lambda_{k,ij} - 3 = \sqrt{(\lambda_{k,ii} - 3)(\lambda_{k,jj} - 3)}, k = r, a \quad (3.15)$$

$$\epsilon_{ij} = (1 - k_{ij}) \frac{\sqrt{\sigma_{ii}^3 \sigma_{jj}^3}}{\sigma_{ij}^3} \sqrt{\epsilon_{ii} \epsilon_{jj}} \quad (3.16)$$

The  $k_{ij}$  is a binary interaction parameter to correct the deviations of the Lorentz-Berthelot rule for chemically distinct compounds. This parameter can be fitted to experimental data or pseudo experimental data.

### 3.1.2 Parameter Estimation for the SAFT- $\gamma$ Mie Force Field

The SAFT- $\gamma$  Mie Force Field uses a coarse graining top down methodology in its parameterization. This methodology aims to obtain the intermolecular parameters from macroscopic experimental data such as fluid-phase equilibrium or interfacial tension data. The idea is that the force field parameters estimated with the SAFT-VR Mie EoS can be used on molecular simulations since both the equation of state and the force field use the same explicit intermolecular potential model (Mie potential). This correspondence between models has already been seen for a variety of fluids in which this force field was parameterized. This success in the representation of the properties of real fluids can be imputed to the degrees of freedom of Mie Potential (HERDES; TOTTON; MÜLLER, 2015). Furthermore, this flexibility provides the exploration of a very large parameter space without using an iterative simulation scheme (AVENDAÑO *et al.*, 2011).

Each substance has initially five parameters to be estimated ( $m_s, \sigma, \epsilon, \lambda_r$  and  $\lambda_a$ ) according to Eq. (3.1). The number of segments are usually fixed in an integer value since each segment represents one pseudo atom. The attractive parameter is generally fixed due to its high correlation with the repulsive parameter. Usually, the parameter



is fixed in the London value of 6, which is a good representation of the dispersion scale of most simple fluids that don't have strong polar interactions (RAMRATTAN *et al.*, 2015; HERDES; TOTTON; MÜLLER, 2015). There are two strategies to obtain the parameters: one is by fitting the Saft-Vr Mie EoS to experimental data as vapor pressure and liquid density and the other one is using correspondent state parametrization. The first, generally, minimizes the following unweighted least-squares objective function:

$$\min_{\sigma, \epsilon, \lambda_r} F_{obj}(\sigma, \epsilon, \lambda_r) = \sum_{i=1}^{N_p} \left( \frac{P_v^{SAFT}(T_i, \sigma, \epsilon, \lambda_r) - P_v^{exp}(T_i)}{P_v^{exp}(T_i)} \right)^2 + \sum_{i=1}^{N_p} \left( \frac{\rho_l^{SAFT}(T_i, \sigma, \epsilon, \lambda_r) - \rho_l^{exp}(T_i)}{\rho_l^{exp}(T_i)} \right)^2 \quad (3.17)$$

where  $N_p$  is the number of experimental points,  $P_v$  is the vapor pressure and  $\rho_l$  is the saturated liquid density. Another properties that can be used in the estimation are superficial tension and speed of sound. The multiple parameters of the model make it necessary the use of a wide range of experimental data since multiple solutions may be found for the fit. Therefore, one needs to be careful in deciding the level of coarse graining (i.e. the parameter  $m_s$ ) and the subsequent parameter space that will not result in some physical inconsistencies such as a premature freezing fluid.

Lafitte *et al.* (2012) suggested that two corrections factors ( $c_\sigma$  and  $c_\epsilon$ ) should be estimated with simulation data when using Eq. (3.12) for the ring contribution. They are related to the EoS parameters by scaled parameters:

$$\sigma^{scaled} = c_\sigma \sigma^{SAFT} \quad (3.18)$$

$$\epsilon^{scaled} = c_\epsilon \epsilon^{SAFT} \quad (3.19)$$

According to Lafitte *et al.* (2012), these corrections are necessary because the approximations employed in the EoS theory generate discrepancies between molecular simulations and the EoS for ring molecules modeled with Eq. (3.12). The objective function for this estimation is given by:

$$\min_{c_\sigma, c_\epsilon} F_{obj}(c_\sigma, c_\epsilon) = \sum_{i=1}^{N_p} \left( \frac{P_v^{sim}(T_i, \sigma^{SAFT}, \epsilon^{SAFT}) - P_v^{SAFT}(T_i, \sigma^{scaled}, \epsilon^{scaled})}{P_v^{sim}(T_i, \sigma^{SAFT}, \epsilon^{SAFT})} \right)^2 + \sum_{i=1}^{N_p} \left( \frac{\rho_{liq}^{sim}(T_i, \sigma^{SAFT}, \epsilon^{SAFT}) - \rho_{liq}^{SAFT}(T_i, \sigma^{scaled}, \epsilon^{scaled})}{\rho_{liq}^{sim}(T_i, \sigma^{SAFT}, \epsilon^{SAFT})} \right)^2 \quad (3.20)$$

The repulsive parameter is maintained in the value found on the minimization of Eq. (3.17). The refined values for  $\sigma$  and  $\epsilon$  are:

$$\sigma^{sim} = \sigma^{SAFT} / c_\sigma \quad (3.21)$$

$$\epsilon^{sim} = \epsilon^{SAFT} / c_\epsilon \quad (3.22)$$

It is interesting to point out that this new parameterization is not necessary when using Eq. (3.13) as the ring contribution. The other method to obtain the force field parameters is the correspondent state parametrization (MEJÍA; HERDES; MÜLLER, 2014). This method considers that the unweighted volume average of the attractive contribution to the Mie intermolecular potential,  $a_1$ , is a mean field approximation:

$$a_1 = 2\pi\rho\sigma^3\epsilon\alpha \quad (3.23)$$

The van der Waals constant,  $\alpha$ , considering  $\lambda_a = 6$  is related by the Mie exponents by:

$$\alpha = \frac{1}{\epsilon\sigma^3} \int_{\sigma}^{\infty} \phi(r)r^2 dr = \frac{\lambda_r}{3(\lambda_r - 3)} \left( \frac{\lambda_r}{6} \right)^{6/(\lambda_r - 6)} \quad (3.24)$$

The parameterization in this method starts by using the experimental acentric factor,  $\omega$ , for each molecule with a fixed value of  $m_s$  to obtain the value of the repulsive exponent with the following Padé series:

$$\lambda_r = \frac{\sum_{i=0} a_i \omega^i}{1 + \sum_{i=1} b_i \omega^i} \quad (3.25)$$

$a_i$  and  $b_i$  are dependent parameters of the number of segments and a table with their values is presented in the original paper (MEJÍA; HERDES; MÜLLER, 2014). The van der Waals constant can be found substituting  $\lambda_r$  into Eq. (3.24). The reduced critical potential  $T_c^*$  is related to  $\alpha$  by a Padé series:

$$T_c^* = \frac{\sum_{i=0} c_i \alpha^i}{1 + \sum_{i=1} d_i \alpha^i} \quad (3.26)$$

The values of  $c_i$  and  $d_i$  are also available in the original paper. The reduced temperature of the equation above is used in conjunction with the experimental critical temperature,  $T_c$ , to find the energy parameter with the relation below:

$$T_c^* = \frac{\kappa_b T_c}{\epsilon} \quad (3.27)$$

The diameter parameter, however, is not obtained with the critical properties, but with the reduced liquid density,  $\rho_{T_r=0.7}$ , at the reduced temperature,  $T_r$ , of 0.7. This density is also obtained with a Padé series using parameters by [Mejía, Herdes and Müller \(2014\)](#):

$$\rho_{T_r=0.7}^* = \frac{\sum_{i=0} j_i \alpha^i}{1 + \sum_{i=1} k_i \alpha^i} \quad (3.28)$$

The relation among the equation above,  $\sigma$  and the experimental density is given by:

$$\rho_{T_r=0.7}^* = \rho_{T_r=0.7} \sigma^3 N_{av} \quad (3.29)$$

where  $N_{av}$  is The Avogadro number. This correspondent state method has the advantage of only requiring critical data, which is available for a great range of fluids, and liquid density data. The parameters found with this strategy are available at an online database ([ERVIK; MEJÍA; MÜLLER, 2016](#)).

The binary interaction parameter  $k_{ij}$  of Eq. (3.16) is necessary to adjust the mixture behavior of chemically distinct components. Normally, it is estimated minimizing the difference between experimental binary vapor liquid equilibrium or interfacial tension data and the SAFT-VR Mie EoS output data ([MÜLLER; MEJÍA, 2017; LOBANOVA et al., 2016](#)). The objective function is similar to:

$$\min_{k_{ij}} F_{obj}(k_{ij}) = \sum_{k=1}^{N_p} \left( \frac{P_v^{SAFT}(T_k, x, k_{ij}) - P_v^{exp}(T_k, x)}{P_v^{exp}(T_k, x)} \right)^2 + \sum_{k=1}^{N_p} \left( \frac{\rho_l^{SAFT}(T_k, x, k_{ij}) - \rho_l^{exp}(T_i)}{\rho_l^{exp}(T_i)} \right)^2 \quad (3.30)$$

However, [Ervik et al. \(2016\)](#) used molecular simulation results to fit the parameter to the superficial tension data. The strategy followed by them was to do simulations in three values of  $k_{ij}$  first and, after, they refined the parameter until a value in good agreement with the experimental data was found.

## 3.2 Molecular Dynamics

## 3.3 Expanded Ensemble Method

Instead of doing various simulations in different values of  $\lambda$ , expanded ensemble simulations ([LYUBARTSEV et al., 1992](#)) were developed to allow a non-Boltzmann

sampling scheme of different states in only one simulation. The statistical expanded ensemble,  $Z^{EE}$  can be defined as a sum of sub ensembles  $Z_i$  in different values of  $\lambda$ :

$$Z^{EE} = \sum_{i=1}^N Z_i(\lambda_i) \exp(\eta_i) \quad (3.31)$$

where  $N$  is the number of alchemical states and  $\eta_i$  is the arbitrary weight of the sub ensemble  $Z_i$  at each state. In solvation energy calculations with molecular dynamics,  $\lambda$  corresponds to the coupling parameter of the soft-core potential (Eq. 2.8) and the expanded ensemble is sampled by performing an arbitrary number of MD steps followed by a  $\lambda$  transition. Chodera and Shirts (2011) proved that the sampling of the expanded ensemble is similar to the Gibbs sampling method (GEMAN; GEMAN, 1984; LIU, 2002). Following the Gibbs method, the sampling of the configuration space  $x$  for one state  $\lambda_k$  during the MD steps is done by using the conditional distribution:

$$\pi(x|\lambda_k) = \frac{\exp[-\beta u(x, \lambda_k)]}{\int dx \exp[-\beta u(x, \lambda_k)]} \quad (3.32)$$

Meanwhile, the state transition in the MD simulation uses the following conditional distribution:

$$\pi(\lambda_k|x) = \frac{\exp[-\beta u(x, \lambda_k) + \eta_k]}{\sum_{k=1}^K \exp[-\beta u(x, \lambda_k) + \eta_k]} \quad (3.33)$$

where  $u(x, \lambda_k) = U(x, \lambda_k) + PV(x, \lambda_k)$  is the reduced potential function for the NPT ensemble. There are a variety of acceptance schemes to do the expanded sampling using Eq. (3.33), but Chodera and Shirts (2011) suggested that the independence sampling (LIU, 2002) is the best strategy to increase the number of uncorrelated configurations. The implementation suggested by them updates the state index from  $i$  to  $j$  by first generating a uniform random number  $R$  on the interval  $[0, 1)$  and then selecting the smallest new value of  $j$  that satisfies the relation below:

$$R < \sum_{i=1}^j \pi(\lambda_i|x) \quad (3.34)$$

The sampling strategy above depends on the weights in order to assure an adequate sampling of the states. If there isn't a sufficient number of states sampled, the expanded ensemble becomes deficient in obtaining input data to estimate free energy differences with the methods exposed in Chapter 2. The weights can be calculated following the flat-histogram approach (BERG; NEUHAUS, 1992; LEE, 1993; DAYAL *et al.*, 2004). This strategy aims to obtain adequate sampling by assuring that all the states have an equal number of samples, i.e. the ratio of the probability of sampling state ( $\pi_i$ )

to the probability of sampling state  $j$  ( $\pi_j$ ) is equal to one. Given that  $\pi_i$  has the following equation:

$$\pi_i = \frac{Z_i(\lambda_i) \exp(\eta_i)}{Z^{EE}} \quad (3.35)$$

and using Eqs. 2.5 and 2.6, the following relation can be obtained for  $\pi_i/\pi_j = 1$ :

$$(\eta_i - \eta_j) = \beta(G_i - G_j) \quad (3.36)$$

Eq. (3.36) is solved iteratively with trial simulations. For the first simulation, the values of  $\eta$  are chosen or set to zero and the histogram of the states visited is obtained. With this histogram, it is possible to estimate the free energy differences and, since the weights are related to the free energies by Eq. (3.36), the next values of  $\eta$  can be calculated. This iteration goes on until a uniform distribution is secured. The weights found are then used in a longer simulation to obtain the final solvation free energy differences.

The choice of the  $\lambda$  set correspondent to overlapping alchemical states are crucial to acquire accurate energy differences. In this work, the method chosen to obtain the optimal stage of the  $\lambda$  domain is the one developed by Escobedo and Martinez-Veracoechea (2007) with basis in the study of Trebst, Huse and Troyer (2004). The method optimizes  $\lambda$  through the minimization of the number of round trips per CPU time between the lowest  $\lambda$  ( $= 0$ ) and highest  $\lambda$  ( $= 1$ ). This is done by maximizing the steady-state stream  $\phi$  of the simulation, which "walks" among the values of  $\lambda$ . This stream is estimated from Fick's diffusion type of law:

$$\phi = D(\Lambda) \Pi(\Lambda) \frac{dx(\Lambda)}{d\Lambda} \quad (3.37)$$

In the equation above,  $\Lambda$  is the actual continue value of the coupling parameter. This continue function of  $\lambda$ s may be obtained by interpolating them linearly.  $D(\Lambda)$  is the diffusivity at state  $\Lambda$  and  $x(\Lambda)$  is the fraction of times that the trial simulation at state  $\Lambda_i$  has most recently visited the state  $\lambda = 1$  as opposed to state  $\lambda = 0$ . The derivative  $dx(\Lambda)/d\Lambda$  can be approximated with the central finite differences method. Finally,  $\Pi(\Lambda)$  is the probability of visiting  $\Lambda$ :

$$\Pi(\Lambda) = \frac{C' \bar{\Pi}(\lambda)}{\Lambda_{i+1} - \Lambda_i} \quad (3.38)$$

The  $C'$  term in the equation above represents a constant and  $\bar{\Pi}(\lambda)$  is the arithmetic

average of visiting the  $\Lambda$  states:

$$\bar{\Pi}(\lambda) = \frac{\pi_{i+1} - \pi_i}{2} \quad (3.39)$$

The  $\phi$  is maximum when the probability  $\Pi'(\Lambda_i)$  is proportional to  $1/\sqrt{D(\Lambda)}$ . With that information, it is possible to estimate the diffusivity using one trial simulation with the following equation:

$$D(\Lambda) = \frac{\Lambda_{i+1} - \Lambda_i}{\bar{\Pi}(\lambda) dx(\Lambda)/d\Lambda} \quad (3.40)$$

Hence, we can calculate  $\bar{\Pi}$  and, consequently, the cumulative probability, which is used to obtain the new  $\lambda$  states:

$$\Phi = \int_{\lambda=0}^{\lambda=1} \Pi'(\Lambda_i) d\Lambda = \frac{i}{K} \quad (3.41)$$

where,  $K$  is the total number of  $\lambda$  states.

### 3.4 Gibbs Ensemble Monte Carlo (GEMC)

The Gibbs Ensemble Method ([PANAGIOTOPOULOS, 1987](#)) is used to study phase coexistence with simultaneous Monte Carlo (MC) simulations of two boxes, representing a two phase system, with periodic conditions. The boxes exchange molecules, energy and volume between them. Equilibrium is obtained through MC steps that consist of translation and rotation moves, volume exchange moves and randomly exchanges of molecules between the boxes. For the phase equilibrium of multi-component systems, the GEMC simulations should be carried out at the NPT (constant number of particles, pressure and temperature) ensemble to obey the requirement of an additional degree of freedom for mixtures. Meanwhile, the simulation of single component systems is carried out at constant number of particles, temperature and volume (NVT) since the two phase region would be a line for this system at constant pressure and temperature. The constant volume GEMC ensemble is rigorously equivalent to the canonical ensemble in the thermodynamic limit as demonstrated by [Frenkel and Smit \(2001\)](#). The partition function of the GEMC-NVT ensemble is obtained considering that the particles in both boxes are subjected to the same intermolecular interactions. Also, the boxes' volumes and number of particles ( $N_1, N_2, V_1$  and  $V_2$ ) can vary while the total volume ( $V$ )

and total number of particles ( $N$ ) remain constant ( $N = N_1 + N_2, V = V_1 + V_2$ ):

$$Q(NVT) \equiv \sum_{N_1}^N \frac{1}{V \Lambda^{3N} N_1! (N - N_1)!} \int_0^V dV_1 V_1^{N_1} V_2^{N_2} \int dx_1^{N_1} \exp[-\beta U(x_1^{N_1})] \int dx_2^{N_2} \exp[-\beta U(x_2^{N_2})] \quad (3.42)$$

In order to define the acceptance rules for the MC moves, it is necessary to know the probability of finding the configuration with  $N_1$  particles in box 1 with volume  $V_1$  and positions  $x_1^{N_1}$  and  $x_2^{N_2}$ . This probability is given by:

$$\pi(x_1^{N_1}, x_2^{N_2}, N_1, N_2, V_1, V_2) \propto \frac{V_1^{N_1} V_2^{N_2}}{N_1! N_2!} \exp[-\beta U(x_1^{N_1}) - \beta U(x_2^{N_2})] \quad (3.43)$$

The acceptance criterion for the translation and rotation moves of configuration A to B is similar to the conventional NVT MC ensembles and is equal to:

$$acc_{A \rightarrow B} = \min(1, \exp[-\beta U(x_A^{N_1}) - \beta U(x_B^{N_1})]) \quad (3.44)$$

The exchange volume moves happen by exchanging an amount  $\Delta V$  between the boxes to achieve pressure equilibrium.  $\Delta V$  can be chosen from a uniform distribution based on the maximum variation of volume defined ( $\delta V_{max}$ ) with probability  $1/\delta V_{max}$ . The acceptance rule for these moves is:

$$acc_{A \rightarrow B} = \min \left( 1, \left( \frac{V_1^B}{V_1^A} \right)^{N_1-1} \left( \frac{V_2^B}{V_2^A} \right)^{N_2+1} \exp[-\beta U(x_A^N) - \beta U(x_B^N)] \right) \quad (3.45)$$

Particle exchange moves are carried out to obtain the equality of chemical potential between the boxes. One particle from one box is removed and then added to a random location in the other box. The criteria to accept or reject this type of move is:

$$acc_{A \rightarrow B} = \min \left( 1, \frac{N_1 V_2}{N_2 V_1} \exp[-\beta U(x_A^N) - \beta U(x_B^N)] \right) \quad (3.46)$$

This method has been widely used to calculate phase equilibrium, but it underperforms for the region near the critical point due to large density fluctuations. The GEMC also has a poor performance for dense systems since the particle exchange moves have a low acceptance ratio for these dense systems.

## 4 Methodology

### 4.1 Phenanthrene Parameterization

The two parameterization strategies for ring molecules described in section 3.1.2 were implemented for phenanthrene. For both of them, only vapor pressure data (MORTIMER; MURPHY, 1923) were used due to the unavailability of saturated liquid density. The attractive parameter,  $\lambda_a$ , was set to six to avoid correlation with the repulsive parameter. The parameterization with the ring equation of Müller and Mejía (2017) was done with the number of segments fixed in 5 since this level of coarse graining was also used for the similar molecule anthracene:

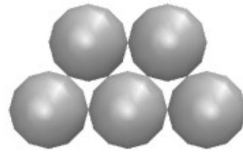


Figure 4.1.1 – Geometry for  $m_s = 5$

The minimization was done using the Particle Swarm Optimization (PSO) method with the following objective function:

$$\min_{\sigma, \epsilon, \lambda_r} F_{obj}(\sigma, \epsilon, \lambda_r) = \sum_{i=1}^{N_p} \left( \frac{P_v^{SAFT}(T_i, \sigma, \epsilon, \lambda_r) - P_v^{exp}(T_i)}{P_v^{exp}(T_i)} \right)^2 \quad (4.1)$$

$P_v^{exp}$  is the experimental vapor pressure and  $P_v^{SAFT}$  is the vapor pressure obtained with SAFT-VR Mie EoS. We used the routine proposed by Smith, Ness and Abbot (2007) routine to calculate the bubble point with the EoS. The resulting parameters  $\sigma$ ,  $\epsilon$  and  $\lambda_r$  of Eq. (4.1) are the final force field parameters used in molecular simulations.

The parameterization with the Lafitte *et al.* (2012) ring equation was done with  $m_s = 3$  so every bead would represent one ring:

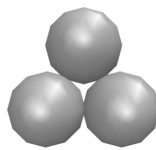


Figure 4.1.2 – Geometry for  $m_s = 3$

The first part of the estimation followed the same procedure described above for the Müller and Mejía (2017) equation. As explained in section 3.1.2, the Lafitte *et al.*



(2012) equation requires the estimation of correction factors  $c_\sigma$  and  $c_\epsilon$  (Eqs. (3.18) and (3.19)). The PSO method was used with Eq. (3.20). In this equation, the vapor pressures and saturated liquid densities from molecular simulations were obtained using the Gibbs Ensemble Monte Carlo method on the NVT ensemble (section 3.4).

The boxes for the GEMC-NVT simulations were generated inserting 400 molecules on the liquid box and 100 on the vapor one using the Packmol package (MARTÍNEZ *et al.*, 2009). Initial densities of each box were equal to the saturated densities found with the SAFT-VR Mie Eos in order to avoid the migration of all molecules to a single phase throughout the simulation. Simulations had equilibration and production times of  $10^4$  and  $510^4$  MC cycles respectively. Each MC cycle corresponded to  $10^3$  rotation trials,  $10^3$  translation trials,  $10^2$  molecule insertion trials,  $10^2$  molecule deletion trials and 10 volume exchange trials. The cut off distance was equal to  $20\text{\AA}$  without long range interactions. The saturated vapor density ( $\rho_{vap}$ ), the saturated liquid density ( $\rho_{liq}$ ) and the vapor pressure ( $P_v$ ) were sampled at each 100 MC cycles and this data were divided in five blocks to calculate the averages and standard deviations. With the correction factors found after the estimations, we calculated the  $\sigma$  and  $\epsilon$  parameters with Eqs. (3.21) and (3.22).

## 4.2 Solvation Free Energy Calculations

Molecular dynamic simulations to estimate the free energy differences with the SAFT- $\gamma$  Mie force field were performed using the Lammmps package (PLIMPTON, 1995). The motion equations were integrated with the velocity-Verlet algorithm (VERLET, 1967) with a time step of 1 fs. As required by the coarse grained model, molecules were treated as rigid bodies. The thermostat and the barostat were the Nose/Hoover with chains with a damping factors of 100 and 1000 fs respectively. Electrostatics interactions are not explicitly accounted by the SAFT- $\gamma$  Mie force field, hence there were no shifting of forces or long range corrections. The potential cutoff was equal to  $20\text{ \AA}$  (MÜLLER; MEJÍA, 2017) with a neighbor skin of  $2\text{ \AA}$ . The initial configurations of the solvated systems were generated with the Packmol package (MARTÍNEZ *et al.*, 2009). For the binary mixtures, one molecule of solute and a varying number of solvent molecules- 700 molecules for toluene and octanol, 1024 for hexane, 3000 for water - were randomly added to a cubic box. The simulations to study solvation free energy of phenanthrene in a mixture of toluene and carbon dioxide were done with different fractions of carbon dioxide. The system consisted of one molecule of phenanthrene for all the fractions and 123 molecules of  $CO_2$  and 618 molecules of toluene for  $w_{CO_2} = 0.087$ ; 166 molecules of  $CO_2$ ; 589 molecules of toluene for  $w_{CO_2} = 0.119$ ; 232 molecules of  $CO_2$  and 545 molecules of toluene for  $w_{CO_2} = 0.169$  and 380 molecules of  $CO_2$  and 446 molecules of toluene for  $w_{CO_2} = 0.289$ .

All simulations were carried out maintaining the temperature and pressure constant at 298 K and 1 bar, except the ones containing carbon dioxide. These had the temperature of 298 K and the pressure of the liquid phase equilibrium correspondent to the  $CO_2$  fraction (CHANG, 1992). For all the simulations, the initial box was equilibrated at the NPT ensemble for 2 ns and then the resulting configurations were used as the initial configuration of the expanded ensemble simulations. These were carried out with the Lammmps user package for expanded ensemble simulations with the Mie Potential developed by our group, available at <https://github.com/atoms-ufjr/USER-ALCHEMICAL>. The sampling of a new state was tried at every 10 MD steps. In order to define the optimal values of  $\lambda$  and  $\eta$  related to each state, short trials simulations, lasting around 10 ns, were carried out. In the first simulation, the group of  $\lambda$  for all the pairs solvent-solute was: (0.0,0.15,0.2,0.25,0.3,0.4,0.45,0.5,0.55,0.7,0.9,1.0) and the  $\eta$ s were set to zero or were given the values of the ones found for similar mixtures. The subsequent groups of  $\eta$  were estimated with the flat histogram approach (Eq. (3.36)). We then used the new weights to optimize the group of  $\lambda$ s by minimizing the number of round trips, as described in section 3.3. The  $\eta$ s correspondent to the newest group of  $\lambda$ s were interpolated from the free energy differences. With the final values of  $\eta$  and  $\lambda$  defined for each mixture, larger simulations with a time of 20 ns were carried out.

Since the force field considers that the beads don't have charges, there is no coulombic interaction and Eq. (2.7) becomes equal to  $\Delta G_{3 \rightarrow 4}$ . The post processing method used to calculate free energy differences was the Multisate Bennet Acceptance Ratio (MBAR) described in section 2.3.4. The software alchemical-analysis (KLIMOVICH; SHIRTS; MOBLEY, 2015) was used to obtain the  $\Delta G_{solv}$  with MBAR and to assess the results quality. We only estimated the binary interaction parameter of Eq. (3.16) for pairs with water as a solvent. The estimation was done by performing trial expanded ensemble simulations in three values of  $k_{ij}$ . With the  $\Delta G_{solv}$  obtained with these simulations, we did a linear fit to obtain the refined value of the parameter. We used this strategy because the estimation with SAFT VR Mie EoS gave poor results for the free energy.

## 5 Results and Discussion

### 5.1 Solvation free energies

The first part of this work consisted of obtaining phenanthrene parameters for the SAFT- $\gamma$  Mie Force Field, as described in section 4.1, since the parameters were not available for the ring geometry on the force field database. The parameters obtained and the mean percentage error (MPE) to the experimental data were:

Table 1 – Estimated SAFT- $\gamma$  Mie Force Field parameters for phenanthrene

$m_s$	$\epsilon/k_B$ (K)	$\sigma(\text{\AA})$	$\lambda_r$	MPE(%)
3 (LAFITTE <i>et al.</i> , 2012)	485.55	4.197	14.34	1.64   9.74
5 (MÜLLER; MEJÍA, 2017)	262.74	4.077	9.55	0.88

In the table above, the first value of MPE for the Lafitte *et al.* (2012) strategy corresponds to the estimation with experimental data and the second corresponds to the corrections factors estimation with MD data. This strategy has an inconsistency of requiring two estimations because parameters solely estimated with the EoS aren't accurate for molecular simulation. Hence, the solvation free energy of phenanthrene was only studied with the set of parameters estimated with Müller and Mejía (2017) strategy. In fact, the (LAFITTE *et al.*, 2012) strategy was only followed because it was the only one available when we first started this work. The sets of parameters for the other compounds were retrieved from the literature (LOBANOVA *et al.*, 2016; HERDES; TOTTON; MÜLLER, 2015; ERVIK; MEJÍA; MÜLLER, 2016; MÜLLER; MEJÍA, 2017):

Table 2 – SAFT- $\gamma$  Mie Force Field for each substance used in this work

	$m_s$	$\epsilon/k_B$ (K)	$\sigma(\text{\AA})$	$\lambda_r$
Water	1	305.21	2.902	8.0
Propane	1	426.08	4.871	34.29
Carbon dioxide	2	194.94	2.848	14.65
Hexane	2	376.35	4.508	19.57
Octanol	3	495.71	4.341	28.79
Toluene	3	268.24	3.685	11.80
Benzene	3	230.30	3.441	10.45
Pyrene	4	459.04	4.134	15.79
Anthracene	5	259.68	3.631	9.55

The solvation free energies of aromatic solutes in nonpolar (hexane), aromatic (toluene) and hydrogen bonding (1-octanol) solvents were examined with binary interaction parameters equal to zero. Since the force field doesn't account for charges, the

solvation free energy is equal to the Mie contribution ( Eq. (2.8)). A total of 15-18  $\lambda$  were used depending on the pairs solute-solvent. The final values of  $\lambda$  were concentrated on the region with a steeper slope. These values and the final values of  $\eta$  are available at Appendix A. The overlapping of the intermediate states are an important measure of the reliability of solvation free energy estimations. In order demonstrate that the group of  $\lambda$  found have a sufficient overlap, the overlapping matrices obtained with the software alchemical-analysis were made available at the Appendix B. The solvation free energies estimated were:

Table 3 – Calculated and experimental values for the solvation free energy differences (kcal/mol) of solutes in non aqueous solvents

Solvent	Solute	$\Delta G_{solv}^{exp}$	$\Delta G_{solv}^{Mie}$	Absolute Deviation
hexane	benzene	-3.96	$-3.76 \pm 0.01$	0.20
hexane	pyrene	-11.53	$-10.82 \pm 0.02$	0.71
hexane	phenanthrene	-10.01	$-9.16 \pm 0.01$	0.85
1-octanol	propane	-1.32	$-1.36 \pm 0.02$	0.04
1-octanol	anthracene	-11.72	$-8.16 \pm 0.03$	3.61
1-octanol	phenanthrene	-10.22	$-8.34 \pm 0.03$	1.47
toluene	pyrene	-12.86	$-11.74 \pm 0.01$	1.11
toluene	anthracene	-11.31	$-9.90 \pm 0.01$	1.41

The absolute deviations are smaller for when the solvent is hexane, what shows that the SAFT- $\gamma$  Mie force field performs better for a non polar solvent. Additionally, this force field presented better results for the pair hexane+benzene than the Trappe force field (GARRIDO *et al.*, 2011). We also can see effect of molecule's size on the entropic region of the free energy curve in Figure 5.1.1. It was expected that a force field based on an EoS that doesn't explicitly account for hydrogen bond would not perform well for 1-octanol. Despite this, the solvation free energies of propane and phenanthrene in 1-octanol stayed in the desired deviation range of 1-2 kcal/mol (MOBLEY; GILSON, 2017). The deviation was much smaller for propane. This can be attributed to propane's non polarity and smoother free energy curve (Figure 5.1.2). The anthracene and phenanthrene molecules have the same geometry in the model and similar physical properties, but the absolute deviation of the solvation free energy of anthracene in 1-octanol is much higher than the one of phenanthrene 1-octanol. This may indicate a problem in the parameterization of anthracene.

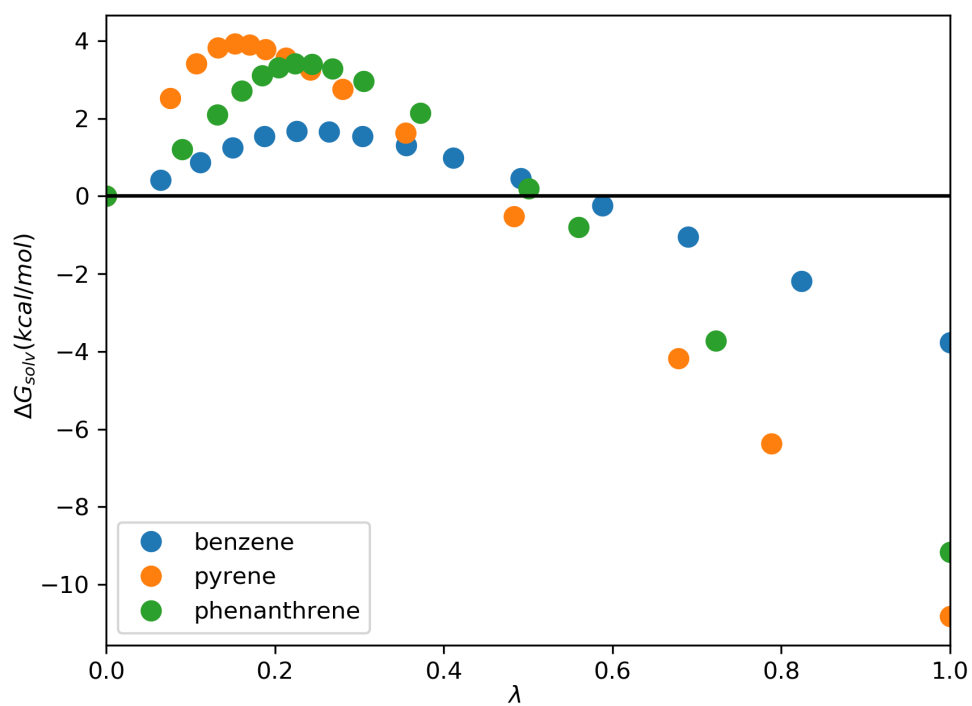


Figure 5.1.1 – Solvation free energy profiles of different solutes in hexane.

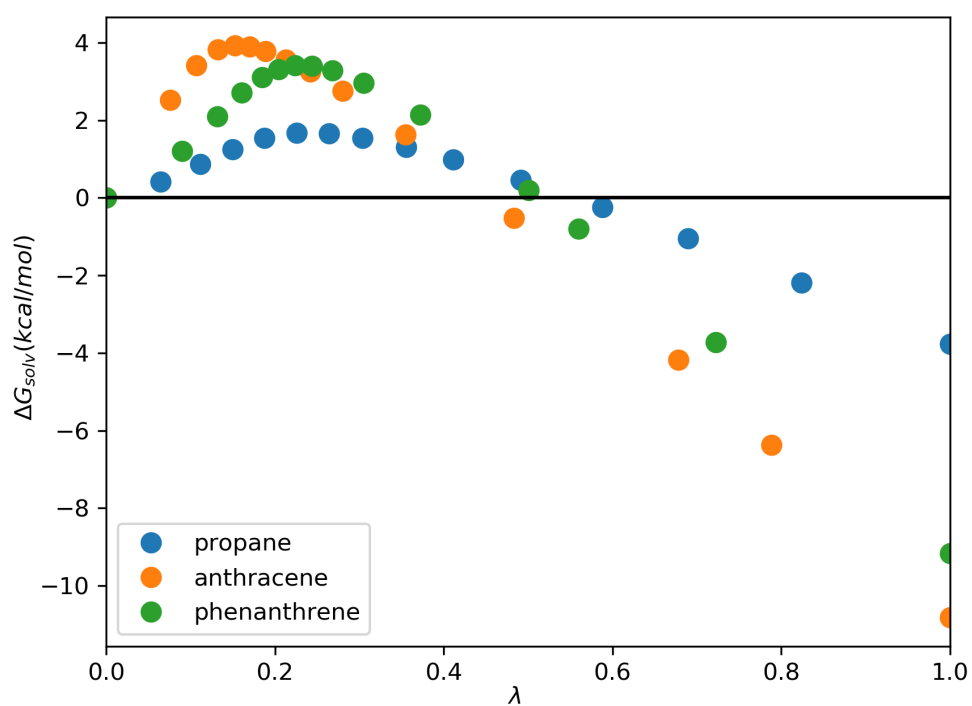


Figure 5.1.2 – Solvation free energy profiles of different solutes in 1-octanol.

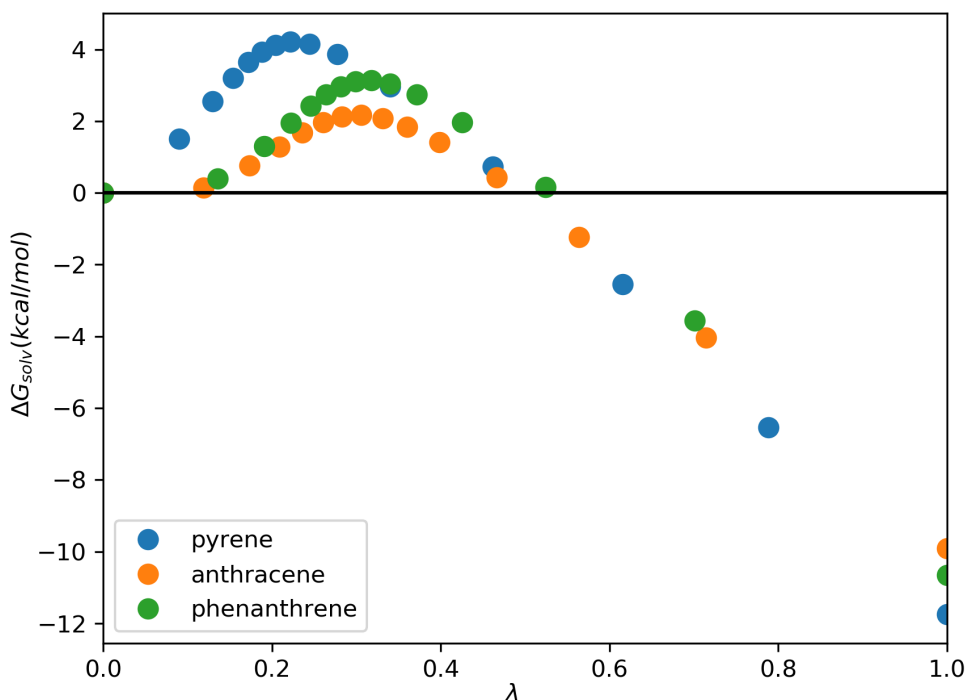


Figure 5.1.3 – Solvation free energy profiles of different solutes in toluene.

The results also indicated the prediction capability of the force field for pairs of aromatic solute and solvent. The influence of the molecule's geometry on free energy curves (Figure 5.1.3) was also observed for these pairs.  $\Delta G_{solv}$  was calculated too for phenanthrene in toluene and in toluene+ $CO_2$ . To the best of our knowledge, there was no available experimental data for these solvation free energies, but the previous results for phenanthrene in other solvents and for the pair anthracene+toluene showed that the force field is adequate to describe the solvation phenomenon of phenanthrene in an aromatic solvent. The results for these sets are exposed below:

Table 4 – Calculated values for the solvation free energy differences (kcal/mol) of phenanthrene in toluene+ $CO_2$ .

$w_{CO_2}$	$\Delta G_{solv}^{Mie}$
0.0	$-10.65 \pm 0.02$
0.087	$-10.73 \pm 0.02$
0.119	$-10.78 \pm 0.02$
0.169	$-10.71 \pm 0.02$
0.289	$-10.69 \pm 0.02$

The increasing of  $CO_2$  mass fraction in toluene caused a small effect on solvation free energies. First, the  $\Delta G_{solv}$  decreased with the increase of  $w_{CO_2}$ , indicating a higher solubility. From the 0.169 fraction, the effect was reversed and carbon dioxide became an

anti solvent. It was observed that asphaltene precipitation occurs when carbon dioxide mass fractions became higher than 0.10 in the system asphaltene+toluene+carbon dioxide (SOROUSH *et al.*, 2014), what is in accordance with the anti solvent effect of carbon dioxide observed on the calculated values. It is also important to point out that the small differences observed in the free energy profiles (Figure 5.1.4) may indicate the non-influence of  $CO_2$  in solvation of phenanthrene in toluene when using the Saft- $\gamma$  Mie force field. But, since this is a qualitative study due the lack of this system experimental data, more studies need to be done in order to make a secure assertion about it.

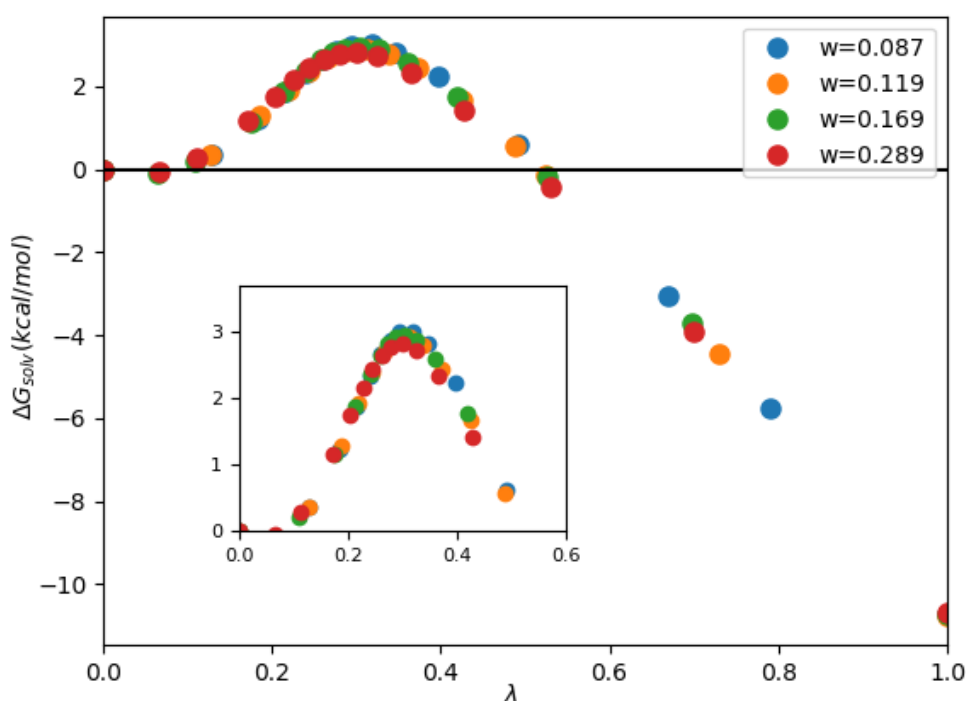


Figure 5.1.4 – Solvation free energy profiles of phenanthrene in toluene+ $CO_2$ .

## 5.2 Hydration free energies

The hydration free energies of widely studied solutes (propane, benzene) and aromatic solutes (toluene, phenanthrene) were calculated with a group of fifteen intermediate states. First, the binary interaction parameter was set to zero, but the results obtained deviated a lot from the experimental data as can be seen in the table below:

Table 5 – Calculated values for the hydration free energy differences (kcal/mol) of solutes in water for  $k_{ij} = 0$ .

Solute	$\Delta G_{solv}^{Mie}$	$\Delta G_{solv}^{exp}$
propane	$2.00 \pm 0.20$	$1.10 \pm 0.01$
benzene	$-0.86 \pm 0.20$	$-4.45 \pm 0.03$
toluene	$-0.83 \pm 0.20$	$-15.80 \pm 0.06$
phenanthrene	$-3.88 \pm 0.60$	$-10.90 \pm 0.04$

After these results, the need of the binary interaction parameter was clear. The  $k_{ij}$  estimation with the SAFT VR Mie EoS and experimental vapor pressure data also didn't provide good results, then the strategy of estimating the  $k_{ij}$  with the output from solvation free energy calculations with molecular dynamics was used, as described in the last paragraph of section 4.2. Individual values for the interaction parameter for each solvent was initially found, but, since the parameters values for aromatic solutes were very similar (0.148, 0.162, 0.152), the average of these values was taken in order to obtain a general parameter for the water+aromatic pairs. The parameters estimated are:

Table 6 – Binary interaction parameters employed.

Pair	$k_{ij}$
water + propane	0.067
water + aromatic	0.154

The relatively large  $k_{ij}$  value for the aromatic solutes can be pinned on the lack of an explicit association term on the model and on the water model itself, since the model didn't need a  $k_{ij}$  for mixtures with 1-octanol. Nevertheless, the value obtained by fitting the parameter with molecular dynamics interfacial tension data was larger for the mixture water+toluene (0.241) (HERDES *et al.*, 2017). The SAFT- $\gamma$  Mie model for water (LOBANOVA *et al.*, 2016) has actually two different of temperature dependent sets of parameters. The one used in this work was the set estimated with experimental interfacial tension data, but the binary interaction parameter estimated with MD phenomenon tension data could not be transferable to solvation free energy calculations. Modeling the water with a coarse grained methodology has a lot of difficulties because the water molecules move independently and only have non bonded interactions (HADLEY; MCCABE, 2010; HADLEY; MCCABE, 2012). The SAFT- $\gamma$  Mie water model considers that one water molecule corresponds to one bead, this strategy only saves small simulation time, but it is able to predict properties at physiological temperatures unlike other more aggressive models, which consider that one bead represents various water molecules. In light of all this, the SAFT- $\gamma$  Mie force field appears to be a good alternative when working close to room temperatures, but the necessity of additional parameters estimated with molecular simulation indicates problems on the model. The solvation



free energy differences calculated with the final fitted binary interaction parameters are presented in Table 7.

Table 7 – Calculated and experimental values for the hydration free energy differences (kcal/mol) of solutes in water.

Solute	$\Delta G_{solv}^{exp}$	$\Delta G_{solv}^{Mie}$	Absolute Deviation	$\Delta G_{solv}^{GAFF}$
propane	$2.00 \pm 0.20$	$2.01 \pm 0.01$	0.01	$2.50 \pm 0.02$
benzene	$-0.86 \pm 0.20$	$-1.12 \pm 0.01$	0.26	$-0.81 \pm 0.02$
toluene	$-0.83 \pm 0.20$	$-0.84 \pm 0.01$	0.01	$-0.79 \pm 0.03$
phenanthrene	$-3.88 \pm 0.60$	$-3.47 \pm 0.02$	0.41	$-5.26 \pm 0.03$

Hydration free energy differences with  $k_{ij}$  had low absolute deviations from the experimental data, as expected since the parameter was adjusted to fit the data. The root mean square error (RMSE) for the pairs tested with the SAFT- $\gamma$  Mie model was equal to 0.24, meanwhile the RMSE for hydration free energy differences with the GAFF force field (MOBLEY; GUTHRIE, 2014) was 0.73. The difference in absolute deviations between the two force fields is significantly high for phenanthrene, hence the coarse grained force field with a binary parameter is preferred if the application requires a higher level of accuracy. Hydration free energy profiles in Figure 5.2.1 show the geometry dependence on the free energy profiles. We can observe also that the solvation free energy for the first non zero lambda is negative for benzene and toluene, when a positive value is expected. This can be caused by numerical errors or by the force field.

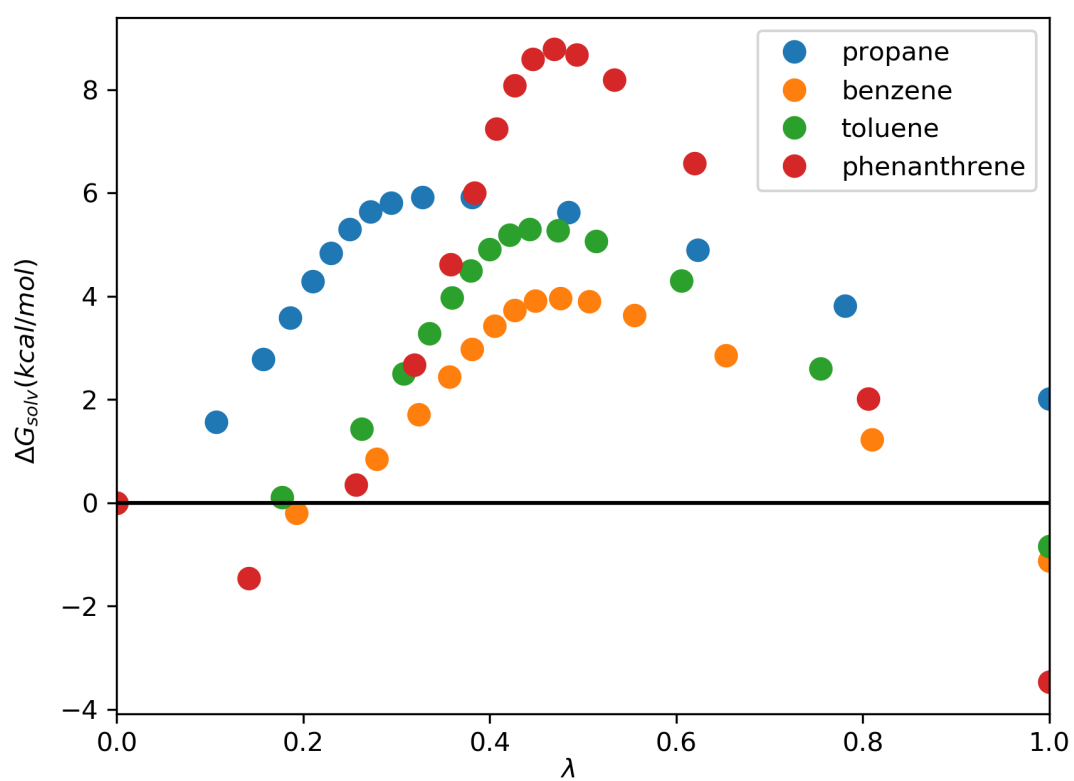


Figure 5.2.1 – Hydration free energy profiles for different solutes.

## 6 Conclusions

This dissertation consisted in the study of solvation free energy calculations of aromatic solutes that can mimic asphaltenes with the SAFT- $\gamma$  Mie force field. By doing that, we provided information about these calculations since solvation free energy studies are mostly done using water as solvent and all atom force fields based on the Lennard Jones Potential. The parametrization of the SAFT- $\gamma$  Mie force field is more straightforward when compared to other force fields since its parameters are obtained through the SAF-VR Mie EoS. Following this strategy, the phenanthrene parameters were obtained using two different ring equations and geometries. The ring equation proposed by Müller and Mejía (2017) provided the more adequate set of parameters. The potential energy data for every intermediate state were obtained with simulations at the expanded ensemble.

Solvation free energy differences were then estimated with these data using the MBAR method. The results for solvation free energy differences with non aqueous solvents had absolute deviations to the experimental data of less than 2.0 kcal/mol, except for the pair 1-octanol+anthracene. The geometry effect on the free energy curves was also observed- larger molecules had steeper curves and larger absolute deviations. The influence of carbon dioxide on the solvation free energy of phenanthrene in toluene was found to be minimum. The  $\Delta G_{solv}$  decreased slightly until the mass fraction of  $CO_2$  was equal to 0.119 and, after this point, solvation free energies increased.

Hydration free energy differences calculations with the SAFT- $\gamma$  Mie model required the use of relatively larger values of  $k_{ij}$  in order to obtain satisfactory results. The parameter was estimated with the output from molecular dynamics data as the strategy of using the SAFT-VR Mie EoS also didn't provide good results. This necessity of one additional parameter happens probably due to the lack of an association term on the EoS that the model is based on. The results with  $k_{ij}$  estimated with MD output were great, the absolute deviations to the experimental data found were smaller than the ones for the GAFF force field.

Generally, the SAFT- $\gamma$  Mie force field proved to be a good model to represent the solvation phenomenon. It correctly described solvation free energy differences of solutes mimicking asphaltenes in hexane, toluene, 1-octanol and water. The requirement of binary interaction parameter estimated with MD output for hydration free energies increases the simulation time, which is already larger for this water model due to its coarse graining level. Nevertheless, the SAFT- $\gamma$  Mie force field for water used doesn't predict freezing at room temperature as other force fields, which is essential

for hydration free energy calculations. This dissertation had success in using a coarse grained force field to perform free energy calculations. Based on this work, we have some ideas for future development. We intend to test the binary interaction parameter transferability to calculations with other aromatic solutes in water. Additionally, we want to use the SAFT- $\gamma$  Mie force field to model more complex asphaltene models and, consequently, increase the scale of these simulations. The final step to expand this work would be to develop new methodologies to use solvation free energies to effectively calculate solubility

# Bibliography

ADAM, L.; MACIEJ, B.; CEZARY, C.; EWA, G.; YI, H.; DAWID, J.; PAWEL, K.; MACIEJ, M.; MARIUSZ, M.; A, M. M.; ANDREI, N.; STANISLAW, O.; A, S. H.; K, S. A.; RAFAL, S.; TOMASZ, W.; YANPING, Y.; BARTLOMIEJ, Z. A unified coarse-grained model of biological macromolecules based on mean-field multipole-multipole interactions. *Journal of molecular modeling*, v. 20, p. 2306, 2014.

AIMOLI, C. G.; MAGINN, E. J.; ABREU, C. Force field comparison and thermodynamic property calculation of supercritical  $CO_2$  and  $CH_4$  using molecular dynamics simulations. *Fluid Phase Equilibria*, v. 368, p. 80–90, 2014.

AIMOLI, C. G.; MAGINN, E. J.; ABREU, C. R. Transport properties of carbon dioxide and methane from molecular dynamics simulations. *The Journal of Chemical Physics*, v. 141, p. 134101, 2014.

AVENDAÑO, C.; LAFITTE, T.; GALINDO, A.; ADJIMAN, C. S.; JACKSON, G.; MULLER, E. A. Soft- $\gamma$  force field for the simulation of molecular fluids.1. a single-site coarse grained model of carbon dioxide. *The Journal of Physical Chemistry B*, v. 115, p. 11154–11169, 2011.

BARDUCCI, A.; BONOMI, M.; DERREUMAUX, P. Assessing the quality of the opep coarse-grained force field. *Journal of Chemical Theory and Computation*, v. 7, p. 1928–1934, 2011.

BARKER, J. A.; HENDERSON, D. What is "liquid"? understanding the states of matter. *Review of Modern Physics*, v. 48, p. 587–671, 1976.

BASDEVANT, N.; BORGIS, D.; HA-DUONG, T. Modeling protein-protein recognition in solution using the coarse-grained force field scorpion. *Journal of Chemical Theory and Computation*, v. 9, p. 803–813, 2013.

BENNETT, C. Efficient estimation of free energy differences from monte carlo data. *Journal of Computational Physics*, v. 22, p. 245–268, 1976.

BEREAU, T.; BACHMANN, M.; DESERNO, M. Interplay between secondary and tertiary structure formation in protein folding cooperativity. *Journal of the American Chemical Society*, v. 132, p. 13129–13131, 2010.

BEREAU, T.; DESERNO, M. Generic coarse-grained model for protein folding and aggregation. *Journal of Chemical Physics*, v. 130, p. 235106, 2009.

BERG, B. A.; NEUHAUS, T. Multicanonical ensemble: A new approach to simulate first-order phase transitions. *Physical Review Letters*, American Physical Society, v. 68, p. 9–12, Jan 1992.

BEUTLER, T.; MARK, A.; SCHAIK, R. van; GERBER, P.; GUNSTEREN, W. van. Avoiding singularities and numerical instabilities in free energy calculations based on molecular simulations. *Chemical Physics Letters*, v. 222, p. 529–539, 1994.

BHARGAVA, B.; KLEIN, M. L. Formation of micelles in aqueous solutions of a room temperature ionic liquid: a study using coarse grained molecular dynamics. *Molecular Simulation*, v. 107, p. 393–401, 2009.

CHANG, C. J. The solubility of carbon dioxide in organic solvents at elevated pressures. *Fluid Phase Equilibria*, v. 15, p. 235–242, 1992.

CHEBARO, Y.; DONG, X.; LAGHAEL, R.; DERREUMAUX, P.; MOUSSEAU, N. Pep-fold: an online resource for de novo peptide structure prediction. *Nucleic Acids Research*, v. 37, p. 498–503, 2009.

CHEBARO, Y.; DONG, X.; LAGHAEL, R.; DERREUMAUX, P.; MOUSSEAU, N. Replica exchange molecular dynamics simulations of coarse-grained proteins in implicit solvent. *Journal of Physical Chemistry B*, v. 113, p. 267–274, 2009.

CHIU, S.; SCOTT, H.; JAKOBSSON, E. A coarse-grained model based on morse potential for water and n-alkanes. *Journal of Chemical Theory and Computation*, v. 6, p. 851–863, 2010.

CHODERA, J. D.; SHIRTS, M. R. Replica exchange and expanded ensemble simulations as gibbs sampling: simple improvements for enhanced mixing. *Journal of Chemical Physics*, v. 135, p. 194110, 2011.

DAYAL, P.; TREBST, S.; WESSEL, S.; WÜRTZ, D.; TROYER, M.; SABHAPANDIT, S.; COPPERSMITH, S. N. Performance limitations of flat-histogram methods. *Physical Review Letters*, American Physical Society, v. 92, p. 097201, Mar 2004.

ERVIK, A.; LYSGAARD, M. O.; HERDES, C.; JIMÉNEZ-SERRATOS, G.; MÜLLER, E. A.; MUNKEJORD, S. T.; MÜLLER, B. A multiscale method for simulating fluid interfaces covered with large molecules such as asphaltenes. *Journal of Computational Physics*, v. 327, p. 576–611, 2016.

ERVIK, A.; MEJÍA, A.; MÜLLER, E. A. Bottled saft: A web app providing saft- $\gamma$  mie force field parameters for thousands of molecular fluids. *Journal of Chemical Information and Modeling*, v. 56, p. 1609–1614, 2016.

ESCOBEDO, F. A.; MARTINEZ-VERACOECHEA, F. J. Optimized expanded ensembles for simulations involving molecular insertions and deletions. i. closed systems. *Journal of Chemical Physics*, v. 127, p. 174103, 2007.

FRENKEL, D.; SMIT, B. *Understanding Molecular Simulation*. 2nd. ed. Orlando, FL, USA: Academic Press, Inc., 2001. ISBN 0122673514.

GARRIDO, N. M.; JORGE, M.; QUEIMADA, A. J.; MACEDO, E. A.; ECONOMOU, I. G. Using molecular simulation to predict solute solvation and partition coefficients in solvents of different polarity. *Physical Chemistry Chemical Physics*, v. 20, p. 9155–9164, 2011.

GARRIDO, N. M.; QUEIMADA, A. J.; JORGE, M.; MACEDO, E. A.; ECONOMOU, I. G. 1-octanol/water partition coefficients of n-alkanes from molecular simulations of absolute solvation free energies. *Journal of Chemical Theory and Computation*, v. 5, p. 2436–2446, 2009.

GEMAN, S.; GEMAN, D. Stochastic relaxation, gibbs distributions, and the bayesian restoration of images. *IEEE Transactions on Pattern Analysis and Machine Intelligence*, PAMI-6, p. 721 – 741, 1984.

GONÇALVES, P. F. B.; STASSEN, H. Free energy of solvation from molecular dynamics simulation applying voronoi-delaunay triangulation to the cavity creation. *The Journal of Chemical Physics*, v. 123, p. 214109, 2005.

HADLEY, K. R.; MCCABE, C. On the investigation of coarse-grained models for water: Balancing computational efficiency and the retention of structural properties. *The Journal of Physical Chemistry B*, v. 114, n. 13, p. 4590–4599, 2010.

HADLEY, K. R.; MCCABE, C. Coarse-grained molecular models of water: A review. *Molecular simulation*, v. 38 8-9, p. 671–681, 2012.

HE, X.; SHINODA, W.; DEVANE, R.; KLEIN, M. L. Exploring the utility of coarse-grained water models for computational studies of interfacial systems. *Molecular Simulation*, v. 108, p. 2007–2020, 2010.

HERDES, C.; ERVIK, A.; MEJÍA, A.; MÜLLER, E. A. Prediction of the water/oil interfacial tension from molecular simulations using the coarse-grained soft- $\gamma$  mie force field. *Fluid Phase Equilib.*, 2017.

HERDES, C.; TOTTON, T. S.; MÜLLER, E. A. Coarse grained force field for the molecular simulation of natural gases and condensates. *Fluid Phase Equilibria*, v. 406, p. 91–100, 2015.

IZAIRI, R.; KAMBERAJ, H. Comparison study of polar and nonpolar contributions to solvation free energy. *Journal of Chemical Information and Modeling*, v. 57, p. 2539–2553, 2017.

JORGE, M.; GARRIDO, N.; QUEIMADA, A.; ECONOMOU, I.; MACEDO, E. Effect of the integration method on the accuracy and computational efficiency of free energy calculations using thermodynamic integration. *Journal of Chemical Theory and Computation*, v. 6, p. 1018–1027, 2010.

KIRKWOOD, J. Statistical mechanics of fluid mixtures. *Journal of Chemical Physics*, v. 3, p. 300–313, 1935.

KLIMOVICH, P. V.; SHIRTS, M. R.; MOBLEY, D. L. Guidelines for the analysis of free energy calculations. *Journal of Computer-Aided Molecular Design*, v. 29, p. 397–411, 2015.

KMIECIK, S.; GRONT, D.; KOLINSKI, M.; WIETESKA, L.; DAWID, A. E.; KOLINSKI, A. Coarse-grained protein models and their applications. *Chemical Reviews*, v. 116, p. 7898–7936, 2016.

KOGA, N.; TAKADA, S. Roles of native topology and chain-length scaling in protein folding: a simulation study with a go-like model. *Journal of Molecular Biology*, v. 331, p. 171–180, 2001.

KUMAR, S.; BOUZIDA, D.; SWENDSEN, R.; KOLLMAN, P.; ROSENBERG, J. The weighted histogram analysis method for free-energy calculations on biomolecules. 1. the method. *Journal of Computational Chemistry*, v. 13, p. 1011–1021, 1992.

LAFITTE, T.; APOSTOLAKOU, A.; AVENDANO, C.; GALINDO, A.; ADJIMAN, C. S.; MULLER, E. A.; JACKSON, G. Accurate statistical associating fluid theory for chain molecules formed from mie segments. *The Journal of Chemical Physics*, v. 139, p. 154504, 2013.

LAFITTE, T.; AVENDAÑO, C.; PAPAIOANNOU, V.; GALINDO, A.; ADJIMAN, C. S.; JACKSON, G.; MÜLLER, E. A. Saft- $\gamma$  force field for the simulation of molecular fluids: 3. coarse-grained models of benzene and hetero-group models of n-decylbenzene. *Molecular Physics*, v. 110, p. 1189–1203, 2012.

LARS, V.; PERIOLE, X.; TIELEMAN, D. P.; MARRINK, S. J. Improved parameters for the martini coarse-grained protein force field. *Journal of Chemical Theory and Computation*, v. 9, p. 687–697, 2013.

LEE, J. New monte carlo algorithm: Entropic sampling. *Physical Review Letters*, American Physical Society, v. 71, p. 211–214, Jul 1993.

LEVITT, M. A simplified representation of protein conformations for rapid simulation of protein folding. *Journal of Molecular Biology*, v. 104, p. 59–107, 1976.

LEVITT, M.; WARSHE, A. Computer-simulation of protein folding. *Nature*, v. 253, p. 694–698, 1975.

LIU, J. S. *Monte Carlo strategies in Scientific Computing*. 2. ed. New York: Springer, 2002.

LOBANOVA, O.; AVENDAÑO, C.; LAFITTE, T.; MÜLLER, E. A.; JACKSON, G. Saft- $\gamma$  force field for the simulation of molecular fluids: 4. a single-site coarse-grained model of water applicable over a wide temperature range. *Mol. Phys.*, v. 113, p. 1228–1249, 2015.

LOBANOVA, O.; MEJÍA, A.; JACKSON, G.; MÜLLER, E. A. Saft- $\gamma$  force field for the simulation of molecular fluids 6: Binary and ternary mixtures comprising water, carbon dioxide, and n-alkanes. *The Journal of Chemical Thermodynamics*, v. 93, p. 320–336, 2016.

LYUBARTSEV, A. P.; MARTSINOVSKI, A. A.; SHEVKUNOV, S. V.; VORONTSOV-VELYAMINOV, P. N. New approach to monte carlo calculation of the free energy: Method of expanded ensembles. *Journal of Chemical Physics*, v. 96, p. 1776–1783, 1992.

MARRINK, S. J.; RISSELADA, H. J.; YEFIMOV, S.; TIELEMAN, D. P.; VRIES, A. H. de. The martini force field: Coarse grained model for biomolecular simulations. *Journal of Physical Chemistry B*, v. 111, p. 7812–7824, 2007.

MARRINK, S. J.; TIELEMAN, D. P. Perspective on the martini model. *Chemical Society Reviews*, v. 42, p. 6801–6822, 2013.

MARTÍNEZ, L.; ANDRADE, R.; BIRGIN, E. G.; MARTÍNEZ, J. M. Packmol: a package for building initial configurations for molecular dynamics simulations. *Journal of Computational Chemistry*, v. 30, p. 2157–2164, 2009.

MATOS, G. D. R.; KYU, D. Y.; LOEFFLER, H. H.; CHODERA, J. D.; SHIRTS, M. R.; MOBLEY, D. L. Approaches for calculating solvation free energies and enthalpies demonstrated with an update of the freesolv database. *Journal Chemical Engineering Data*, v. 62, p. 1559–1569, 2017.



- MEJÍA, A.; HERDES, C.; MÜLLER, E. A. Force fields for coarse-grained molecular simulations from a corresponding states correlation. *Industrial and Chemical Engineering Research*, v. 53, p. 4131–4141, 2014.
- MIE, G. Zur kinetischen theorie der einatomigen korper. *Ann. Phys.*, v. 316, p. 657–697, 1903.
- MOBLEY, D. L.; DUMONT, E.; CHODERA, J. D.; DILL, K. A. Comparison of charge models for fixed-charge force fields: Small-molecule hydration free energies in explicit solvent. *The Journal of Physical Chemistry B*, v. 111, n. 9, p. 2242–2254, 2007.
- MOBLEY, D. L.; GILSON, M. K. Predicting binding free energies: Frontiers and benchmarks. *Annual Review of Biophysics*, v. 46, n. 1, p. 531–558, 2017.
- MOBLEY, D. L.; GUTHRIE, J. P. Freesolv: a database of experimental and calculated hydration free energies, with input files. *Journal of computer-aided molecular design*, v. 28, n. 7, p. 711–720, July 2014. ISSN 0920-654X.
- MOHAMED, N. A.; BRADSHAW, R. T.; ESSEX, J. W. Evaluation of solvation free energies for small molecules with the amoeba polarizable force field. *Journal of Computational Chemistry*, v. 37, p. 2749–2758, 2016.
- MORTIMER, S.; MURPHY, R. The vapor pressures of some substances found in coal tar. *Industrial and Engineering Chemistry Research*, v. 14, p. 1140–1142, 1923.
- MÜLLER, E. A.; GUBBINS, K. E. Simulation of hard triatomic and tetratomic molecules. a test of associating fluid theory. *Molecular Physics*, v. 80, p. 957–976, 1993.
- MÜLLER, E. A.; MEJÍA, A. Extension of the soft-vr mie eos to model homonuclear rings and its parametrization based on the principle of corresponding states. *Langmuir*, -, p. A–L, 2017.
- PALIWAL, H.; SHIRTS, M. R. A benchmark test set for alchemical free energy transformations and its use to quantify error in common free energy methods. *Journal of Chemical Theory and Computation*, v. 7, p. 4115–4134, 2011.
- PANAGIOTOPOULOS, A. Direct determination of phase coexistence properties of fluids using *Molecular Physics*, v. 61, p. 813–826, 1987.
- PANTANO, D.; KLEIN, M. L. Characterization of membrane-protein interactions for the leucine transporter from aquifex aeolicus by molecular dynamics calculations. *Journal of Physical Chemistry B*, v. 113, p. 13715–13722, 2009.
- PAPAIIOANNOU, V.; LAFITTE, T.; AVENDAÑO, C.; ADJIMAN, C. S.; JACKSON, G.; MÜLLER, E. A.; GALINDO, A. Group contribution methodology based on the statistical associating fluid theory for heteronuclear molecules formed from mie segments. *The Journal of Chemical Physics*, v. 140, p. 054107, 2014.
- PLIMPTON, S. Fast parallel algorithms for short-range molecular dynamics. *Journal of Computational Physics*, v. 117, p. 1–19, 1995.
- POHORILLE, A.; JARZYNSKI, C.; CHIPOT, C. Good practices in freeenergy calculations. *Journal of Physical Chemistry B*, v. 114, p. 10235–10253, 2010.

RAMRATTAN, N.; AVENDAÑO, C.; MÜLLER, E.; GALINDO, A. A corresponding-states framework for the description of the mie family of intermolecular potentials. *Molecular Physics*, v. 113, p. 1–16, 2015.

ROWLINSON, J. S.; SWINTON, F. L. *Liquid and Liquid Mixtures*. 3. ed. London: Butterworth Scientific, 1982.

ROY, D.; BLINOV, N.; KOVALENKO, A. Predicting accurate solvation free energy in n-octanol using 3d-rism-kh molecular theory of solvation: Making right choices. *Journal of Physical Chemistry B*, v. 121, p. 9268–9273, 2017.

SHINODA, W.; DEVANE, R.; KLEIN, M. L. Multi-property fitting and parameterization of a coarse grained model for aqueous surfactants. *Molecular Simulation*, v. 33, p. 27–36, 2007.

SHINODA, W.; DEVANE, R.; KLEIN, M. L. Zwitterionic lipid assemblies: molecular dynamics studies of monolayers, bilayers, and vesicles using a new coarse grain force field. *Journal of Physical Chemistry B*, v. 114, p. 6836–6849, 2010.

SHIRTS, M. R.; CHODERA, J. D. Statistically optimal analysis of samples from multiple equilibrium states. *Journal of Chemical Physics*, v. 129, p. 124105, 2008.

SHIRTS, M. R.; PITERA, J. W.; SWOPE, W. C.; PANDE, V. S. Extremely precise free energy calculations of amino acid side chain analogs: Comparison of common molecular mechanics force fields for proteins. *Journal of Chemical Physics*, v. 119, p. 5740, 2003.

SHYU, C.; YTREBERG, F. M. Reducing the bias and uncertainty of free energy estimates by using regression to fit thermodynamic integration data. *Journal of Computational Chemistry*, v. 6, p. 1018–1027, 2010.

SJÖBLOM, J.; ASKE, N.; AUFLEM, I. H.; BRANDAL Øystein; HAVRE, T. E.; SæTHER Øystein; WESTVIK, A.; JOHNSEN, E. E.; KALLEVIK, H. Our current understanding of water-in-crude oil emulsions.: Recent characterization techniques and high pressure performance. *Advances in Colloid and Interface Science*, v. 100-102, n. Supplement C, p. 399 – 473, 2003. ISSN 0001-8686.

SJÖBLOM, J.; SIMON, S.; XU, Z. Model molecules mimicking asphaltene. *Advances in Colloid and Interface Science*, v. 218, n. Supplement C, p. 1 – 16, 2015. ISSN 0001-8686.

SMITH, J.; NESS, H. V.; ABBOT, M. M. *Introdução á Termodinâmica da Engenharia Química*. 2. ed. Rio de Janeiro: LTC, 2007.

SORROUSH, S.; STRAVER, E. J.; RUDOLPH, E. S. J.; PETERS, C. J.; LOOS, T. W. de; ZITHA, P. L.; VAFAIE-SEFTI, M. Phase behavior of the ternary system carbon dioxide+toluene+asphaltene. *Fuel*, v. 137, n. Supplement C, p. 405 – 411, 2014. ISSN 0016-2361.

STERPONE, F.; DERREUMAUX, P.; MELCHIONNA, S. Protein simulations in fluids: Coupling the opep coarse-grained force field with hydrodynamics. *ga*, v. 11, p. 1843–1853, 2015.

STERPONE, F.; MELCHIONNA, S.; TUFFERY, P.; PASQUALI, S.; MOUSSEAU, N.; CRAGNOLINI, T.; CHEBARO, Y.; ST-PIERRE, J.-F.; KALIMERI, M.; BARDUCCI, A.; LAURIN, Y.; TEK, A.; BAADEN, M.; NGUYEN, P. H.; DERREUMAUX, P. The opep protein model: from single molecules, amyloid formation, crowding and hydrodynamics to dna/rna systems. *Chemical Society Reviews*, v. 43, p. 4871–4893, 2014.

TORRIE, G.; VALLEAU, J. Nonphysical sampling distributions in monte carlo free-energy estimation: Umbrella sampling. *Journal of Computational Physics*, v. 23, n. 2, p. 187 – 199, 1977. ISSN 0021-9991.

TREBST, S.; HUSE, D. A.; TROYER, M. Optimizing the ensemble for equilibration in broad-histogram monte carlo simulations. *Physical Review E*, American Physical Society, v. 70, p. 046701, Oct 2004.

VERLET, L. Computer "experiments" on classical fluids. i. thermodynamical properties of lennard-jones molecules. *Physical Review*, v. 159, p. 98–103, 1967.

WINGER, M.; TRZESNIAK, D.; BARON, R.; GUNSTEREN, W. van. On using a too large integration time step in molecular dynamics simulations of coarse-grained molecular models. *Physical Chemistry Chemical Physics*, v. 11, p. 1934, 2009.

ZWANZIG, R. W. High-temperature equation of state by a perturbation method. i. nonpolar gases. *The Journal of Chemical Physics*, v. 22, p. 1420, 1954.

ZWANZIG, R. W. High-temperature equation of state by a perturbation method. ii. polar gases. *The Journal of Chemical Physics*, v. 23, p. 1915, 1955.

# Appendix

# APPENDIX A – Optimized values of $\lambda$ and $\eta$

Table 8 – Optimized values of  $\lambda$  and  $\eta$  for the solutes in hexane

benzene		pyrene		phenanthrene	
$\lambda$	$\eta$	$\lambda$	$\eta$	$\lambda$	$\eta$
0.000	0.000	0.000	0.000	0.000	0.000
0.065	0.708	0.076	4.234	0.090	1.981
0.112	1.385	0.107	5.620	0.132	3.461
0.150	1.892	0.132	6.499	0.161	4.494
0.188	2.399	0.152	6.690	0.185	5.185
0.226	2.519	0.170	6.643	0.205	5.552
0.264	2.457	0.189	6.461	0.224	5.725
0.304	2.367	0.213	6.091	0.244	5.722
0.356	1.921	0.242	5.566	0.268	5.523
0.411	1.411	0.280	4.729	0.305	4.975
0.492	0.524	0.355	2.853	0.372	3.576
0.588	-0.663	0.483	-0.778	0.500	0.297
0.690	-2.016	0.678	-6.947	0.560	-1.390
0.824	-3.922	0.788	-10.631	0.722	-6.309
1.000	-6.583	1.000	-18.141	1.000	-15.448

Table 9 – Optimized values of  $\lambda$  and  $\eta$  for the solutes in 1-octanol

propane		anthracene		phenanthrene	
$\lambda$	$\eta$	$\lambda$	$\eta$	$\lambda$	$\eta$
0.000	0.000	0.000	0.000	0.000	0.000
0.027	3.126	0.078	3.932	0.049	2.578
0.050	5.109	0.111	6.178	0.091	5.663
0.073	6.093	0.130	7.426	0.125	8.575
0.095	6.570	0.143	8.201	0.144	10.069
0.117	6.826	0.154	8.717	0.157	10.978
0.142	6.956	0.164	9.085	0.169	11.599
0.174	6.969	0.174	9.357	0.180	12.040
0.215	6.847	0.184	9.556	0.192	12.340
0.269	6.554	0.197	9.676	0.206	12.499
0.337	6.050	0.214	9.681	0.225	12.478
0.427	5.228	0.238	9.490	0.253	12.161
0.545	3.955	0.274	8.958	0.298	11.280
0.720	1.843	0.326	7.906	0.371	9.406
1.000	-1.903	0.399	6.088	0.484	5.891
		0.515	2.777	0.664	-0.516
		0.695	-2.960	0.802	-5.908
		1.000	-13.768	1.000	-14.073

Table 10 – Optimized values of  $\lambda$  and  $\eta$  for the solutes in toluene

pyrene		anthracene		phenanthrene	
$\lambda$	$\eta$	$\lambda$	$\eta$	$\lambda$	$\eta$
0.000	0.000	0.000	0.000	0.000	0.000
0.090	2.563	0.119	0.218	0.136	0.726
0.130	4.338	0.174	1.210	0.191	2.307
0.154	5.439	0.209	2.052	0.223	3.430
0.172	6.181	0.236	2.664	0.246	4.233
0.188	6.670	0.261	3.122	0.264	4.780
0.204	6.986	0.283	3.378	0.281	5.149
0.222	7.121	0.306	3.449	0.299	5.354
0.244	7.025	0.332	3.311	0.318	5.389
0.278	6.520	0.360	2.936	0.340	5.222
0.340	5.010	0.399	2.209	0.372	4.717
0.462	1.247	0.466	0.567	0.425	3.440
0.616	-4.283	0.564	-2.211	0.524	0.444
0.788	-11.032	0.715	-6.983	0.701	-5.814
1.000	-19.814	1.000	-16.923	1.000	-17.803

Table 11 – Optimized values of  $\lambda$  and  $\eta$  for the phenanthrene in different mass fractions of  $CO_2$  in toluene

0.087		0.119		0.169		0.289	
$\lambda$	$\eta$	$\lambda$	$\eta$	$\lambda$	$\eta$	$\lambda$	$\eta$
0.000	0.000	0.000	0.000	0.000	0.000	0.000	0.000
0.128	0.604	0.128	0.732	0.064	0.883	0.066	0.806
0.184	2.067	0.186	2.223	0.108	0.764	0.111	0.760
0.217	3.164	0.219	3.319	0.175	1.969	0.172	1.983
0.240	3.940	0.244	4.098	0.214	3.156	0.204	2.967
0.260	4.472	0.267	4.704	0.240	3.974	0.227	3.627
0.277	4.823	0.289	5.031	0.258	4.457	0.245	4.082
0.295	5.035	0.313	5.084	0.273	4.750	0.262	4.395
0.318	5.059	0.339	4.950	0.287	4.921	0.279	4.583
0.347	4.762	0.373	4.371	0.305	4.962	0.299	4.621
0.397	3.753	0.425	3.055	0.326	4.885	0.325	4.423
0.491	1.031	0.488	1.196	0.361	4.401	0.365	3.739
0.670	-5.148	0.525	-0.027	0.419	2.990	0.428	2.198
0.791	-9.713	0.730	-7.185	0.527	-0.299	0.530	-0.842
1.000	-18.098	1.000	-17.769	0.697	-6.180	0.701	-6.763
				1.000	-17.998	1.000	-18.163

Table 12 – Optimized values of  $\lambda$  and  $\eta$  for the solutes in water

propane		benzene		toluene		phenanthrene	
$\lambda$	$\eta$	$\lambda$	$\eta$	$\lambda$	$\eta$	$\lambda$	$\eta$
0.000	0.000	0.000	0.000	0.000	0.000	0.000	0.000
0.107	2.673	0.193	-0.295	0.177	0.182	0.142	-2.462
0.157	4.703	0.279	1.468	0.262	2.432	0.256	0.597
0.186	6.047	0.324	2.931	0.307	4.244	0.319	4.504
0.210	7.148	0.357	4.168	0.336	5.552	0.358	7.762
0.230	8.017	0.381	5.091	0.360	6.696	0.384	10.104
0.250	8.883	0.405	5.891	0.380	7.558	0.407	12.185
0.272	9.291	0.427	6.443	0.400	8.233	0.427	13.607
0.294	9.700	0.449	6.770	0.422	8.678	0.446	14.490
0.328	9.900	0.476	6.900	0.443	8.859	0.469	14.834
0.381	9.930	0.506	6.805	0.473	8.810	0.494	14.667
0.484	9.463	0.555	6.392	0.514	8.452	0.533	13.832
0.623	8.195	0.653	5.109	0.606	7.148	0.620	11.069
0.781	6.378	0.810	2.421	0.755	4.273	0.806	3.279
1.000	3.333	1.000	-1.480	1.000	-1.547	1.000	-6.122

## APPENDIX B – Overlapping Matrices

$\lambda$	0	1	2	3	4	5	6	7	8	9	10	11	12	13	14
0	.42	.29	.16	.08	.03	.01	.01								
1	.33	.27	.18	.10	.06	.03	.02	.01							
2	.23	.23	.18	.12	.09	.06	.04	.02	.01	.01					
3	.14	.16	.16	.13	.11	.10	.08	.06	.03	.02	.01				
4	.06	.09	.11	.11	.12	.12	.13	.11	.07	.04	.02	.01	.01		
5	.02	.03	.05	.07	.09	.12	.16	.16	.12	.08	.05	.02	.01	.01	
6		.01	.02	.03	.06	.09	.15	.18	.16	.12	.08	.04	.02	.01	
7			.01	.02	.03	.07	.13	.17	.18	.16	.11	.07	.04	.02	.01
8				.01	.02	.04	.09	.14	.17	.18	.15	.10	.06	.03	.01
9					.01	.02	.06	.11	.15	.18	.17	.13	.09	.05	.02
10						.01	.04	.07	.11	.16	.18	.17	.14	.08	.03
11						.01	.02	.04	.08	.12	.17	.19	.19	.14	.06
12							.01	.02	.05	.08	.13	.18	.22	.19	.11
13							.01	.01	.03	.05	.09	.15	.22	.25	.19
14								.01	.01	.03	.06	.11	.19	.29	.30

Figure B.0.1 – Overlapping matrix for hexane+benzene.



$\lambda$	0	1	2	3	4	5	6	7	8	9	10	11	12	13	14
0	.75	.19	.05	.01											
1	.28	.33	.19	.09	.05	.03	.02	.01							
2	.08	.21	.19	.15	.12	.10	.07	.04	.02	.01					
3	.01	.08	.11	.13	.14	.15	.15	.11	.07	.03	.01				
4		.03	.05	.08	.12	.16	.18	.16	.12	.07	.03	.01			
5		.01	.02	.05	.09	.14	.18	.18	.15	.10	.05	.01			
6			.01	.03	.07	.12	.17	.19	.18	.13	.07	.02			
7				.02	.04	.09	.14	.19	.20	.16	.11	.04	.01		
8				.01	.03	.06	.12	.17	.20	.19	.15	.06	.01		
9					.02	.04	.08	.14	.19	.20	.19	.09	.02	.01	
10					.01	.02	.05	.09	.14	.19	.25	.17	.06	.03	
11						.01	.02	.04	.07	.11	.21	.27	.17	.09	.01
12								.01	.02	.03	.08	.18	.32	.29	.07
13									.01	.01	.03	.10	.30	.38	.16
14											.01	.03	.16	.36	.44

Figure B.0.2 – Overlapping matrix for hexane+pyrene.

$\lambda$	0	1	2	3	4	5	6	7	8	9	10	11	12	13	14
0	.54	.29	.11	.04	.01										
1	.29	.31	.19	.11	.05	.03	.01	.01							
2	.14	.25	.20	.15	.10	.07	.04	.02	.01						
3	.06	.15	.17	.16	.14	.11	.09	.06	.04	.02					
4	.02	.07	.11	.13	.14	.13	.13	.11	.09	.05	.02				
5	.01	.03	.06	.09	.12	.13	.14	.14	.13	.10	.04	.01			
6		.01	.03	.05	.08	.11	.13	.15	.17	.16	.07	.02	.01		
7			.01	.03	.05	.08	.11	.15	.19	.21	.12	.03	.02		
8				.01	.03	.05	.08	.12	.19	.25	.17	.06	.03		
9					.01	.02	.05	.09	.16	.26	.24	.10	.06	.01	
10						.01	.02	.04	.09	.20	.27	.19	.14	.03	
11								.01	.03	.08	.17	.28	.28	.13	.02
12									.01	.04	.12	.27	.31	.20	.03
13										.01	.04	.17	.27	.37	.14
14											.01	.05	.09	.31	.55

Figure B.0.3 – Overlapping matrix for hexane+phenanthrene.

$\lambda$	0	1	2	3	4	5	6	7	8	9	10	11	12	13	14
0	.66	.26	.06	.01											
1	.40	.30	.14	.08	.04	.02	.01								
2	.10	.14	.17	.22	.15	.09	.06	.03	.02	.01					
3	.01	.03	.09	.20	.20	.16	.12	.08	.05	.03	.01	.01			
4		.01	.05	.14	.18	.17	.15	.12	.08	.05	.03	.01	.01		
5			.02	.09	.15	.16	.16	.14	.11	.08	.04	.02	.01		
6			.01	.06	.11	.14	.15	.16	.13	.11	.06	.04	.02	.01	
7			.01	.04	.07	.11	.13	.16	.15	.14	.09	.06	.03	.01	
8				.02	.05	.07	.10	.14	.16	.17	.13	.09	.05	.02	
9				.01	.02	.04	.07	.11	.14	.18	.16	.14	.09	.03	.01
10					.01	.02	.04	.07	.10	.16	.18	.18	.15	.06	.01
11					.01	.01	.02	.04	.06	.11	.15	.21	.24	.13	.02
12							.01	.02	.03	.06	.10	.19	.30	.24	.05
13								.01	.01	.02	.05	.11	.26	.38	.16
14										.01	.02	.04	.13	.34	.47

Figure B.0.4 – Overlapping matrix for 1-octanol+propane.

$\lambda$	0	1	2	3	4	5	6	7	8	9	10	11	12	13	14	15	16	17
0	.57	.28	.09	.03	.01	.01												
1	.28	.32	.17	.09	.06	.03	.02	.01	.01									
2	.13	.25	.19	.12	.09	.07	.05	.04	.03	.02	.01							
3	.06	.17	.17	.13	.11	.09	.07	.06	.05	.04	.03	.01						
4	.03	.11	.13	.12	.11	.10	.09	.08	.08	.06	.05	.03	.01					
5	.01	.07	.10	.10	.10	.10	.09	.09	.09	.09	.08	.05	.02	.01				
6	.01	.04	.07	.07	.08	.09	.09	.10	.11	.11	.10	.07	.04	.02				
7		.02	.04	.05	.07	.08	.08	.10	.11	.12	.13	.10	.06	.03	.01			
8		.01	.02	.03	.05	.06	.07	.09	.11	.13	.15	.13	.09	.04	.01			
9			.01	.02	.03	.04	.05	.07	.10	.13	.17	.16	.12	.06	.02	.01		
10				.01	.02	.02	.04	.05	.08	.11	.17	.19	.16	.10	.04	.01		
11					.01	.01	.02	.03	.05	.09	.14	.19	.20	.15	.07	.02		
12							.01	.01	.03	.05	.10	.17	.22	.21	.13	.05	.01	
13								.01	.01	.03	.06	.11	.19	.25	.22	.11	.02	
14										.01	.02	.05	.12	.21	.29	.22	.06	
15											.01	.02	.04	.11	.24	.36	.21	.01
16													.01	.03	.09	.28	.49	.10
17															.01	.06	.33	.59

Figure B.0.5 – Overlapping matrix for 1-octanol+anthracene.

$\lambda$	0	1	2	3	4	5	6	7	8	9	10	11	12	13	14	15	16	17
0	.51	.34	.11	.03	.01													
1	.37	.36	.17	.06	.02	.01												
2	.22	.32	.23	.12	.06	.03	.02	.01										
3	.10	.20	.22	.18	.11	.07	.05	.03	.02	.01	.01							
4	.04	.12	.16	.18	.13	.11	.08	.07	.05	.03	.02	.01						
5	.02	.06	.10	.14	.13	.12	.10	.10	.09	.07	.05	.02	.01					
6	.01	.03	.06	.10	.11	.11	.11	.11	.11	.10	.08	.05	.02					
7		.01	.03	.06	.07	.09	.09	.11	.13	.13	.13	.09	.05	.01				
8			.01	.03	.04	.06	.07	.10	.13	.14	.17	.14	.09	.02				
9				.01	.02	.03	.05	.07	.11	.14	.19	.19	.15	.04				
10					.01	.01	.02	.04	.07	.11	.19	.23	.22	.07	.01			
11							.01	.02	.04	.07	.15	.23	.30	.14	.02			
12								.01	.02	.04	.09	.18	.35	.24	.06	.01		
13										.01	.03	.10	.28	.34	.16	.06	.01	
14											.01	.03	.12	.27	.28	.23	.06	
15													.02	.06	.14	.44	.31	.03
16														.01	.04	.33	.49	.13
17															.01	.13	.45	.41

Figure B.0.6 – Overlapping matrix for 1-octanol+phenanthrene.

$\lambda$	0	1	2	3	4	5	6	7	8	9	10	11	12	13	14
0	.53	.30	.11	.04	.01	.01									
1	.21	.34	.22	.12	.06	.03	.01	.01							
2	.09	.25	.24	.16	.11	.07	.04	.02	.01						
3	.04	.17	.20	.17	.14	.11	.08	.05	.03	.01					
4	.02	.10	.15	.15	.14	.13	.11	.09	.07	.04	.01				
5	.01	.05	.10	.12	.13	.13	.13	.12	.11	.08	.02				
6		.02	.05	.08	.10	.12	.13	.14	.15	.14	.05	.01			
7		.01	.02	.04	.06	.09	.11	.14	.19	.21	.11	.02			
8			.01	.02	.03	.05	.08	.12	.19	.27	.18	.05	.01		
9					.01	.02	.04	.07	.15	.29	.28	.10	.02		
10							.01	.03	.08	.22	.35	.23	.06	.01	
11								.01	.02	.08	.22	.38	.22	.07	.01
12										.02	.07	.25	.37	.25	.05
13											.01	.07	.26	.45	.20
14												.01	.08	.36	.55

Figure B.0.7 – Overlapping matrix for toluene+pyrene.

$\lambda$	0	1	2	3	4	5	6	7	8	9	10	11	12	13	14
0	.48	.29	.14	.05	.02	.01									
1	.24	.30	.23	.12	.06	.03	.01								
2	.12	.24	.24	.17	.11	.06	.03	.02	.01						
3	.06	.16	.21	.19	.14	.09	.07	.04	.02	.01					
4	.03	.10	.16	.17	.15	.12	.10	.07	.05	.03	.02				
5	.01	.05	.10	.13	.14	.13	.13	.11	.09	.06	.04	.01			
6		.02	.05	.08	.10	.11	.13	.13	.12	.11	.09	.03	.01		
7		.01	.02	.04	.06	.08	.11	.13	.15	.15	.15	.07	.02		
8			.01	.02	.03	.05	.08	.11	.14	.18	.21	.12	.05	.01	
9				.01	.01	.02	.05	.08	.12	.18	.26	.18	.08	.02	
10						.01	.02	.04	.08	.15	.27	.24	.14	.04	
11							.01	.02	.04	.09	.21	.28	.25	.10	.01
12								.01	.01	.04	.12	.23	.33	.23	.03
13										.01	.04	.11	.28	.41	.14
14												.02	.08	.29	.60

Figure B.0.8 – Overlapping matrix for toluene+anthracene.

$\lambda$	0	1	2	3	4	5	6	7	8	9	10	11	12	13	14
0	.52	.31	.11	.04	.01										
1	.20	.34	.23	.12	.06	.03	.01	.01							
2	.07	.24	.25	.17	.11	.07	.04	.02	.01						
3	.03	.15	.21	.18	.14	.11	.07	.05	.03	.01	.01				
4	.01	.09	.16	.16	.15	.13	.11	.08	.06	.03	.02				
5		.05	.11	.13	.14	.13	.13	.11	.09	.06	.04	.01			
6		.02	.06	.09	.11	.12	.13	.13	.12	.10	.08	.03	.01		
7		.01	.03	.05	.08	.10	.12	.13	.14	.14	.13	.07	.02		
8			.01	.03	.04	.07	.09	.11	.14	.16	.18	.13	.04		
9				.01	.02	.04	.06	.08	.12	.16	.22	.20	.07	.01	
10					.01	.01	.03	.05	.08	.13	.24	.29	.14	.02	
11							.01	.02	.04	.08	.19	.34	.26	.07	
12									.01	.03	.09	.25	.39	.22	.01
13											.02	.07	.25	.53	.13
14													.03	.27	.69

Figure B.0.9 – Overlapping matrix for toluene+phenanthrene.



$\lambda$	0	1	2	3	4	5	6	7	8	9	10	11	12	13	14
0	.54	.30	.11	.04	.01										
1	.23	.34	.23	.11	.05	.03	.01	.01							
2	.09	.25	.25	.17	.10	.06	.04	.02	.01						
3	.04	.16	.22	.18	.13	.10	.08	.05	.03	.01					
4	.02	.10	.16	.17	.14	.12	.11	.08	.05	.03	.01				
5	.01	.05	.11	.13	.13	.13	.13	.12	.09	.06	.03				
6		.02	.06	.10	.11	.12	.14	.14	.13	.11	.06	.01			
7		.01	.03	.06	.07	.10	.13	.14	.15	.16	.11	.03			
8			.01	.02	.04	.06	.09	.13	.16	.21	.20	.07	.01		
9				.01	.01	.03	.05	.08	.13	.22	.29	.14	.02		
10						.01	.02	.03	.07	.17	.35	.27	.06	.02	
11								.01	.02	.07	.24	.39	.19	.07	.01
12										.01	.05	.19	.37	.32	.07
13											.01	.07	.29	.43	.20
14												.01	.11	.34	.54

Figure B.0.10 – Overlapping matrix for toluene+ $CO_2$ (0.087)+phenanthrene.

$\lambda$	0	1	2	3	4	5	6	7	8	9	10	11	12	13	14
0	.55	.31	.10	.03	.01										
1	.24	.36	.22	.10	.05	.02	.01								
2	.09	.27	.26	.17	.10	.06	.03	.01	.01						
3	.04	.17	.22	.18	.14	.10	.07	.04	.02	.01					
4	.01	.09	.16	.17	.15	.14	.12	.08	.05	.03	.01				
5		.04	.09	.12	.13	.15	.15	.12	.10	.07	.03	.01			
6		.01	.04	.07	.10	.12	.15	.15	.15	.12	.06	.02	.01		
7			.01	.03	.05	.08	.12	.14	.17	.19	.12	.05	.03		
8				.01	.02	.04	.08	.11	.17	.22	.19	.09	.05	.01	
9					.01	.02	.03	.06	.12	.22	.26	.16	.10	.01	
10							.01	.02	.06	.15	.27	.24	.19	.04	
11								.01	.03	.09	.22	.28	.26	.11	.01
12								.01	.02	.06	.18	.28	.28	.16	.01
13										.01	.05	.13	.18	.48	.14
14											.01	.02	.03	.32	.62

Figure B.0.11 – Overlapping matrix for toluene+ $CO_2$ (0.119)+phenanthrene.

$\lambda$	0	1	2	3	4	5	6	7	8	9	10	11	12	13	14	15
0	.32	.36	.24	.06	.02											
1	.24	.34	.27	.09	.03	.01	.01									
2	.18	.30	.28	.13	.06	.02	.01	.01								
3	.08	.19	.24	.19	.12	.06	.04	.03	.02	.01						
4	.03	.10	.16	.19	.16	.10	.08	.06	.05	.03	.02	.01				
5	.01	.05	.09	.14	.15	.12	.11	.09	.08	.07	.05	.02	.01			
6	.01	.03	.05	.10	.12	.11	.11	.11	.11	.10	.08	.05	.02			
7		.01	.03	.07	.09	.09	.11	.11	.12	.12	.11	.08	.04	.01		
8		.01	.01	.04	.06	.07	.09	.11	.12	.13	.14	.12	.07	.01		
9				.02	.03	.05	.07	.09	.11	.14	.16	.17	.13	.03		
10				.01	.01	.02	.04	.06	.08	.12	.17	.21	.21	.06	.01	
11						.01	.02	.03	.05	.08	.14	.23	.31	.12	.02	
12								.01	.02	.03	.07	.18	.37	.24	.07	
13										.01	.02	.07	.26	.37	.25	.01
14												.01	.07	.24	.55	.12
15													.01	.04	.30	.66

Figure B.0.12 – Overlapping matrix for toluene+ $CO_2$ (0.169)+phenanthrene.

$\lambda$	0	1	2	3	4	5	6	7	8	9	10	11	12	13	14	15
0	.33	.33	.22	.07	.02	.01										
1	.25	.31	.25	.11	.05	.02	.01									
2	.17	.27	.26	.15	.08	.04	.02	.01								
3	.08	.17	.22	.20	.13	.09	.05	.03	.02	.01						
4	.04	.10	.15	.19	.16	.12	.09	.07	.04	.03	.01	.01				
5	.02	.06	.10	.15	.15	.13	.11	.10	.07	.05	.03	.02				
6	.01	.03	.06	.11	.13	.13	.12	.12	.09	.08	.06	.03	.01			
7		.01	.03	.07	.10	.11	.12	.12	.11	.11	.10	.07	.03	.01		
8		.01	.01	.04	.07	.09	.10	.12	.12	.14	.13	.11	.05	.01		
9				.02	.04	.05	.07	.09	.11	.14	.17	.17	.10	.03		
10				.01	.01	.02	.04	.06	.08	.12	.17	.23	.18	.06	.01	
11						.01	.01	.02	.04	.08	.14	.25	.28	.14	.03	
12								.01	.01	.03	.07	.19	.33	.27	.08	
13										.01	.02	.09	.25	.38	.23	.02
14												.02	.08	.27	.50	.12
15													.01	.05	.30	.65

Figure B.0.13 – Overlapping matrix for toluene+ $CO_2(0.289)$ +phenanthrene.

$\lambda$	0	1	2	3	4	5	6	7	8	9	10	11	12	13	14
0	.45	.28	.16	.08	.02	.01									
1	.24	.26	.24	.16	.06	.02	.01	.01							
2	.13	.21	.26	.21	.09	.05	.02	.02	.01						
3	.07	.16	.24	.23	.12	.06	.04	.03	.03	.01					
4	.04	.11	.21	.22	.13	.08	.05	.05	.06	.04	.01				
5	.02	.07	.16	.19	.12	.08	.06	.08	.10	.08	.03	.01			
6	.01	.04	.09	.13	.09	.07	.07	.10	.16	.16	.07	.02			
7		.01	.04	.06	.05	.05	.06	.10	.20	.24	.14	.04	.01		
8			.01	.02	.03	.03	.04	.09	.20	.29	.19	.07	.02		
9				.01	.01	.01	.02	.06	.17	.29	.25	.13	.03	.01	
10							.01	.03	.11	.24	.28	.21	.08	.02	
11								.01	.04	.12	.21	.31	.22	.09	.01
12									.01	.03	.08	.22	.33	.26	.07
13										.01	.02	.08	.25	.40	.25
14												.02	.08	.31	.59

Figure B.0.14 – Overlapping matrix for water+propane.

$\lambda$	0	1	2	3	4	5	6	7	8	9	10	11	12	13	14
0	.44	.33	.16	.05	.02	.01									
1	.19	.32	.27	.13	.05	.03	.01								
2	.08	.23	.30	.19	.10	.06	.03	.01	.01						
3	.04	.16	.27	.20	.13	.09	.05	.03	.02	.01					
4	.02	.10	.21	.19	.14	.11	.08	.06	.04	.03	.02				
5	.01	.06	.15	.16	.13	.12	.11	.08	.07	.06	.04	.01			
6		.03	.08	.11	.11	.11	.11	.10	.10	.10	.09	.04	.01		
7		.01	.04	.06	.07	.08	.10	.10	.12	.14	.16	.09	.02		
8			.01	.03	.04	.05	.07	.09	.11	.17	.23	.15	.05	.01	
9				.01	.01	.02	.04	.06	.09	.16	.27	.22	.09	.02	
10						.01	.02	.03	.06	.14	.27	.27	.14	.04	.01
11							.01	.01	.03	.09	.23	.29	.23	.08	.01
12									.01	.04	.12	.22	.31	.22	.06
13										.01	.03	.08	.22	.39	.28
14												.02	.07	.29	.62

Figure B.0.15 – Overlapping matrix for water+benzene.

$\lambda$	0	1	2	3	4	5	6	7	8	9	10	11	12	13	14
0	.46	.32	.15	.04	.01										
1	.19	.31	.28	.13	.06	.02	.01								
2	.07	.21	.32	.20	.11	.05	.02	.01							
3	.03	.13	.28	.23	.15	.08	.05	.03	.01	.01					
4	.01	.08	.23	.22	.17	.11	.07	.05	.03	.02	.01				
5	.01	.05	.16	.19	.16	.12	.09	.07	.05	.04	.03	.01			
6		.02	.10	.14	.14	.12	.11	.09	.08	.08	.07	.03	.01		
7		.01	.05	.08	.09	.10	.10	.10	.11	.12	.14	.08	.02		
8			.01	.03	.05	.06	.07	.09	.11	.15	.22	.16	.04	.01	
9				.01	.02	.03	.04	.06	.09	.14	.27	.24	.08	.01	
10						.01	.02	.03	.06	.12	.27	.31	.15	.03	
11							.01	.01	.03	.08	.23	.33	.23	.07	.01
12									.01	.03	.12	.25	.34	.22	.03
13										.01	.03	.08	.24	.45	.19
14												.01	.04	.25	.69

Figure B.0.16 – Overlapping matrix for water+toluene.

$\lambda$	0	1	2	3	4	5	6	7	8	9	10	11	12	13	14
0	.50	.37	.10	.02											
1	.29	.38	.23	.08	.02										
2	.08	.21	.33	.26	.10	.03	.01								
3	.02	.07	.24	.34	.22	.09	.02	.01							
4		.02	.13	.31	.29	.16	.07	.02	.01						
5		.01	.06	.22	.29	.20	.12	.06	.03	.01					
6			.02	.12	.21	.21	.17	.12	.08	.04	.02	.01			
7			.01	.04	.11	.14	.16	.16	.15	.11	.09	.04			
8				.01	.03	.06	.09	.13	.17	.17	.19	.14	.02		
9						.01	.03	.06	.11	.16	.26	.30	.06		
10							.01	.02	.05	.11	.25	.43	.13	.01	
11									.01	.05	.17	.48	.27	.02	
12										.01	.05	.29	.48	.15	.01
13												.03	.17	.58	.22
14													.01	.24	.75

Figure B.0.17 – Overlapping matrix for water+phenanthrene.